Prepared under contract 01-CCOS

CALCULATION OF PHOTOLYSIS RATE PARAMETERS FROM CCOS ACTINIC FLUX DATA

William R. Stockwell

Division of Atmospheric Sciences, Desert Research Institute
2215 Raggio Parkway, Reno, NV 89512-1095

Prepared for:
California Air Resources Board
and the California Environmental Protection Agency
P.O. Box 2815
Sacramento CA 95812

Under Subcontract to:
San Joaquin Valleywide Air Pollution Study Agency

August 12, 2003

DISCLAIMER

The statements and conclusions in this report are those of the contractor and not necessarily those of the California Air Resources Board. The mention of commercial products, their source, or their use in connection with material reported herein is not to be construed as actual or implied endorsement of such products.

ACKNOWLEDGEMENTS

This report was submitted in fulfillment of (ARB contract 01-CCOS, Advanced Data Analysis - Phase 1) by the Desert Research Institute under a subcontract to the University of California, Davis, sponsored by the California Air Resources Board. Work was completed as of August, 11, 2003.

The author acknowledges the helpful contributions of John Carroll and Mike Mata, University of California at Davis; Rainer Schmitt, Metcon; Eric Fujita, Wendy Goliff and Dongchul Kim, Desert Research Institute; and Jian Zhang, Truckee Meadows Community College.

ABSTRACT

The photolysis of nitrogen dioxide and ozone are processes that drive the formation of photochemical air pollution. However most field studies do not include accurate characterization of their photolysis rate parameters. More often photolysis rate parameters are estimated from model calculations or inferred from flat plate radiometer measurements. Photolysis rate parameters are functions of the actinic flux which is the spherically integrated photon flux, and this cannot be measured by flat plate spectral-radiometers. Uncertainties in photolysis rate parameters estimated from models or flat plate radiometers may be as high as ±40%. To overcome this problem, spectral-radiometers consisting of a 2π radiation collection head attached to a diode array spectrometer were used to make actinic flux measurements during the Central California Ozone Study (CCOS) that was conducted during summer, 2000. The spectral-radiometers were located at Sunol, CA; the University of California (UC-Davis); and Desert Research Institute (DRI) in Reno, NV. The Sunol spectrometer was located at the CCOS-supersite and provided actinic flux taken near the Pacific coast. The instrument at UC-Davis provided actinic flux data that is probably more representative of the overall CCOS domain and the instrument was co-located with a station of the U.S. Department of Agriculture - UVB Radiation Monitoring Program. The instrument located at DRI provided data that was typical of the Sierra Mountains. The spectral-radiometer at UC-Davis operated from July 14 to October 25, the spectral-radiometer at Sunol operated from July 19 to September 22 and the third operated at DRI from August 29 to November 14. An analysis of the photolysis rate parameters for ozone, nitrogen dioxide and formaldehyde based on the measured actinic flux, standard quantum yields and absorption cross section data are presented in this report. These values have an uncertainty of ~ 30%. The rate parameters were compared with simulated values and in every case the simulation was greater than the values derived from the measurements. The differences were greater for the July-August episode than for the September episode. The simulated and measured photolysis rate parameters of NO_2 were in closer agreement than the photolysis rate parameters of O_3 and HCHO. In spite of experimental uncertainties it seems likely that the actual photolysis rate parameters are lower then those currently used by air quality models. This may have consequences for future regulatory modeling.

TABLE OF CONTENTS

1. Introduction 1

2. Setup of Spectral-Radiometers at Measurement Sites 3

3. Calibration of Spectral-Radiometers 6

4. Calculation of 2π Actinic Flux from Spectral-Radiometer Measurements 11

5. Determination of Albedo Correction Function 15

6. Calculation of Photolysis Rate Parameters from 4π Actinic Flux 22

7. Comparison of Photolysis Rate Parameters with Model Values and Discussion of Results 27

8. Conclusions 48

9. References 49

Appendix A Description of Photolysis Rate Parameter Data Files 50

LIST OF FIGURES

Figure 1-1. Flat plate radiometer measurements depend on the solar zenith angle 2

Figure 1-2. Actinic photon flux is total flux entering a spherical volume element of air 2

Figure 2-1. Spectral-radiometer solar radiation collection head 4

Figure 2-2. Locations of actinic flux measurement sites 4

Figure 2-3. Setup of the spectral-radiometer at University of California at Davis, Sunol and DRI. The arrow at DRI points to the spectral-radiometer location 5

Figure 3-1. Calibration setup for spectral-radiometers 6

Figure 3-2. Irradiance spectrum of the standard calibration lamp 6

Figure 3-3. Original average calibration spectra produced by calibration procedure 7

Figure 3-4. Actinic flux at Noon Aug 31, 2000 with original calibration used for Sunol data 8

Figure 3-5. Actinic flux for a hemispheres sampling head calculated with Madronich radiative transfer model 8

Figure 3-6. Sunol instrument was moved to UC Davis site and both instruments were compared; plot for 09/27/2000, 12:44:08 pm 9

Figure 3-7. Sunol revised calibration based on intercomparison with instrument at UC-Davis 10

Figure 3-8. Sunol instrument was recalibrated to match UC-Davis instrument; plot for 09/27/2000, 12:44:08 pm. The solid black line represents the recalibrated Sunol spectral-radiometer data and the crossed red line represents the UC-Davis spectral-radiometer data 10

Figure 4-1. Hemispheric actinic flux measured at noon from the Sunol and UC-Davis sites for July 30 to August 2 given per 1 nm spectral intervals 13

Figure 4-2. Hemispheric actinic flux measured at noon from all three sites for September 17 to 21 given per 1 nm spectral intervals 14

Figure 5-1. Ratio of photon counts measured by spectral-radiometer at UC-Davis to those measured by spectral-radiometer Sunol@Davis 16

Figure 5-2. Standard deviation of ratio of photon counts measured by spectral-radiometer at UC-Davis to those measured by spectral-radiometer Sunol@Davis expressed as a percent 16

Figure 5-3. Albedo correction function calculated for September 28, 2000 18

Figure 5-4. Albedo correction function calculated for October 5, 2000 18

Figure 5-5. Albedo correction function calculated for October 12, 2000 19

Figure 5-6. Total albedo correction function calculated for October 17, 2000 19

Figure 5-7. Average albedo correction function 20

Figure 5-8. Standard deviation of albedo correction function expressed as a percent 20

Figure 5-9. Smoothed average albedo correction function 21

Figure 7-1. Photolysis rate parameters of NO_2 measured at UC-Davis and Sunol for episode July 30 to August 2, 2000 31

Figure 7-2. Simulated photolysis rate parameters of NO_2 at UC-Davis and Sunol for episode July 30 to August 2, 2000 31

Figure 7-3. Photolysis rate parameters of NO_2 measured at UC-Davis, Sunol and DRI for episode September 17 to 21, 2000 32

Figure 7-4. Simulated photolysis rate parameters of NO_2 at UC-Davis, Sunol and DRI for episode September 17 to 21, 2000 32

Figure 7-5. Photolysis rate parameters of O_3 measured at UC-Davis and Sunol for episode July 30 to August 2, 2000 33

Figure 7-6. Simulated rate parameters of O_3 at UC-Davis and Sunol for episode July 30 to August 2, 2000 33

Figure 7-7. Photolysis rate parameters of O_3 measured at UC-Davis, Sunol and DRI for episode September 17 to 21, 2000 34

Figure 7-8. Simulated photolysis rate parameters of O_3 at UC-Davis, Sunol and DRI for episode September 17 to 21, 2000 34

Figure 7-9. Ratio of photolysis rate parameters of O_3 to photolysis rate parameters of NO_2 measured at UC-Davis and Sunol for episode July 30 to August 2 35

Figure 7-10. Simulated ratio of photolysis rate parameters of O_3 to photolysis rate parameters of NO_2 at UC-Davis and Sunol for episode July 30 to August 2 35

Figure 7-11. Ratio of photolysis rate parameters of O_3 to photolysis rate parameters of NO_2 measured at UC-Davis, Sunol and DRI for episode September 17 to 21 36

Figure 7-12. Simulated ratio of photolysis rate parameters of O_3 to photolysis rate parameters of NO_2 at UC-Davis, Sunol and DRI for episode September 17 to 21 36

Figure 7-13. Photolysis rate parameters of HCHO reaction to form molecular products measured at UC-Davis and Sunol for episode July 30 to August 2, 2000 37

Figure 7-14. Simulated photolysis rate parameters of HCHO reaction to form molecular products at UC-Davis and Sunol for episode July 30 to August 2, 2000 37

Figure 7-15. Photolysis rate parameters of HCHO reaction to form molecular products measured at UC-Davis, Sunol and DRI for episode September 17 to 21, 2000 38

Figure 7-16. Simulated photolysis rate parameters of HCHO reaction to form molecular products at UC-Davis, Sunol and DRI for episode September 17 to 21, 2000 38

Figure 7-17. Ratio of photolysis rate parameters of HCHO reaction to form molecular products to photolysis rate parameters of NO_2 measured at UC-Davis and Sunol for episode July 30 to August 2, 2000 39

Figure 7-18. Simulated ratio of photolysis rate parameters of HCHO reaction to form molecular products to photolysis rate parameters of NO_2 at UC-Davis and Sunol for episode July 30 to August 2, 2000 39

Figure 7-19. Ratio of photolysis rate parameters of HCHO reaction to form molecular products to photolysis rate parameters of NO_2 measured at UC-Davis, Sunol and DRI for episode September 17 to 21, 2000 40

Figure 7-20. Simulated ratio of photolysis rate parameters of HCHO reaction to form molecular products to photolysis rate parameters of NO_2 at UC-

Davis and Sunol for UC-Davis, Sunol and DRI for episode September 17 to 21, 2000 40

Figure 7-21. Photolysis rate parameters of HCHO reaction to form radical products measured at UC-Davis and Sunol for episode July 30 to August 2, 2000 41

Figure 7-22. Simulated photolysis rate parameters of HCHO reaction to form radical products at UC-Davis and Sunol for episode July 30 to August 2, 2000 41

Figure 7-23. Photolysis rate parameters of HCHO reaction to form radical products measured at UC-Davis, Sunol and DRI for episode September 17 to 21, 2000 42

Figure 7-24. Simulated photolysis rate parameters of HCHO reaction to form radical products at UC-Davis, Sunol and DRI for episode September 17 to 21, 2000 42

Figure 7-25. Ratio of photolysis rate parameters of HCHO reaction to form radical products to photolysis rate parameters of NO_2 measured at UC-Davis and Sunol for episode July 30 to August 2, 2000 43

Figure 7-26. Simulated ratio of photolysis rate parameters of HCHO reaction to form radical products to photolysis rate parameters of NO_2 at UC-Davis and Sunol for episode July 30 to August 2, 2000 43

Figure 7-27. Ratio of photolysis rate parameters of HCHO reaction to form radical products to photolysis rate parameters of NO_2 measured at UC-Davis, Sunol and DRI for episode September 17 to 21, 2000 44

Figure 7-28. Simulated ratio of photolysis rate parameters of HCHO reaction to form radical products to photolysis rate parameters of NO_2 at UC-Davis and Sunol for UC-Davis, Sunol and DRI for episode September 17 to 21, 2000 44

Figure 7-29. Shadowband radiometer data at a wavelength of 300 nm from UC-Davis site for episode July 30 to August 2. The data is provided by the U.S. Department of Agriculture UV-B Monitoring and Research Program, Natural Resource Ecology Laboratory, Colorado State University 46

Figure 7-29. Shadowband radiometer data at a wavelength of 300 nm from UC-Davis site for the episode September 17 to 21. The data is provided by the U.S. Department of Agriculture UV-B Monitoring and Research Program, Natural Resource Ecology Laboratory, Colorado State University 46

LIST OF TABLES

Table 6-1. Sources of cross sections and quantum yields used 22

Table 6-2. Average absorption cross section of NO_2 used in this work 23

Table 6-3. Average quantum yield of NO_2 used in this work 23

Table 6-4. Average absorption cross section of O_3 used in this work 24

Table 6-5. Average quantum yield of O_3 used in this work 24

Table 6-6. Average absorption cross section of HCHO used in this work 25

Table 6.7. Average quantum yield of HCHO + hν → H_2 + CO used in this work 25

Table 6-8. Average quantum yield of HCHO + hν (+O_2)→ HO_2 + CO used in this work 26

Table 7-1. Median maximum photolysis rate parameters measured and simulated for the episode July 30 to August 20 and their percent differences (using the measurements as reference values) 45

Table 7-2. Ratio of median maximum photolysis rate parameters to the photolysis rate parameter of NO_2 measured and simulated for the episode July 30 to August 20 and their percent differences (using the measurements as reference values) 45

Table 7-3. Median maximum photolysis rate parameters measured and simulated for the episode September 17-21 and their percent differences (using the measurements as reference values) 47

Table 7-4. Ratio of median maximum photolysis rate parameters to the photolysis rate parameter of NO_2 measured and simulated for the episode September 17-21 and their percent differences (using the measurements as reference values). 47

Table A-1. Reactions and files provided with report 50

Table A-2. Format of photolysis rate parameter files. File JNO2_July_UC_Davis used as an example 50

1. Introduction

The photolysis of nitrogen dioxide, ozone, formaldehyde and other carbonyl containing compounds are the initial steps in the production of photochemical air pollutants (Finlayson-Pitts and Pitts, 1999). Unfortunately photolytic rate parameters are not measured in most field studies. They are often estimated from models that assume standard atmospheric conditions or estimated from flat plate radiometer measurements. The problem with modeled photolytic rate parameters is that standard atmospheric conditions usually are not representative of the meteorological conditions of the real field study. Flat plate radiometers have a cosine response that depends on the solar zenith angle, Figure 1-1, and it is not easy to convert these measurements to spherically integrated actinic flux and this is critical because photolysis rate are parameters depend upon spherically integrated actinic flux, Figure 1-2, and not upon irradiance. Uncertainties in photolysis rate parameters estimated from flat plate radiometers may be uncertain within a factor of ±40% or more. Given this uncertainty it is not possible to evaluate the photolytic rate parameters used in air quality models.

To overcome these problems measurements of spectrally resolved actinic flux are required. Diode array spectrometers are available that are capable of making actinic flux measurements during the Central California Ozone Study (CCOS). The photolysis rate of an air pollutant is the product of the compounds mixing ratio and its photolytic rate parameter. Photolysis rate parameters were calculated according to Equation 1-1 (Jacobson, 1999) for NO_2, O_3 and HCHO.

$$J = \sum I(\lambda) \times \sigma(\lambda) \times \phi(\lambda) \times \Delta\lambda \qquad (1\text{-}1)$$

where $I(\lambda)$ is the actinic flux in the wavelength interval $\Delta\lambda$, $\sigma(\lambda)$ is the average absorption cross section of the chemical species in the wavelength interval $\Delta\lambda$ and $\Phi(\lambda)$ is the average quantum yield for the reaction in the wavelength interval $\Delta\lambda$.

The photolytic rate parameter is the integral over all wavelengths of the product of the compound's absorption cross section, quantum yield and actinic flux. A compound's absorption cross section and quantum yield are available from laboratory studies. The actinic flux can be measured with a diode array spectrometer that has a hemispheric sampling head (2π response), Figure 3. The advantage of a diode array spectrometer is that the actinic flux measurements can be used to calculate the photolysis rate of any compound provided that its absorption cross sections and quantum yields are known. The rate parameters for the following reactions were calculated from the measured actinic flux.

$NO_2 + h\nu \rightarrow NO + (O^3P)$		(1-2)
$O_3 + h\nu \rightarrow O_2 + O(^1D)$		(1-3)
$HCHO + h\nu \rightarrow H_2 + CO$	"Molecular Reaction"	(1-4)
$HCHO + h\nu\ (+O_2) \rightarrow 2\ HO_2 + CO$	"Radical Reaction"	(1-5)

Figure 1-1. Flat plate radiometer measurements depend on the solar zenith angle.

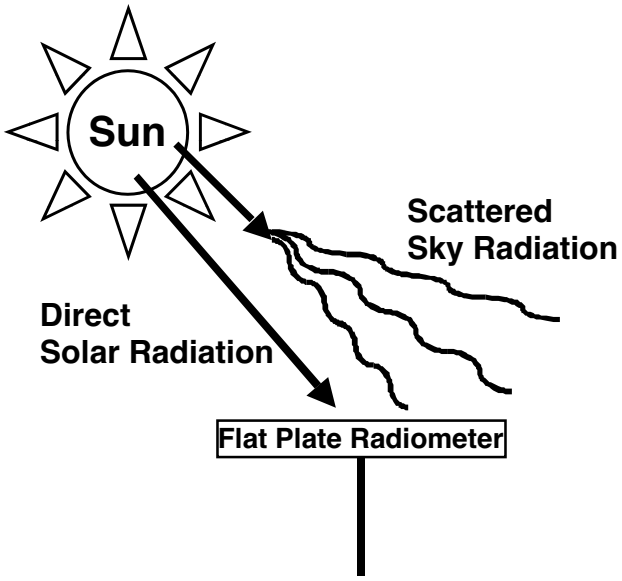

Figure 1-2. Actinic photon flux is total flux entering a spherical volume element of air.

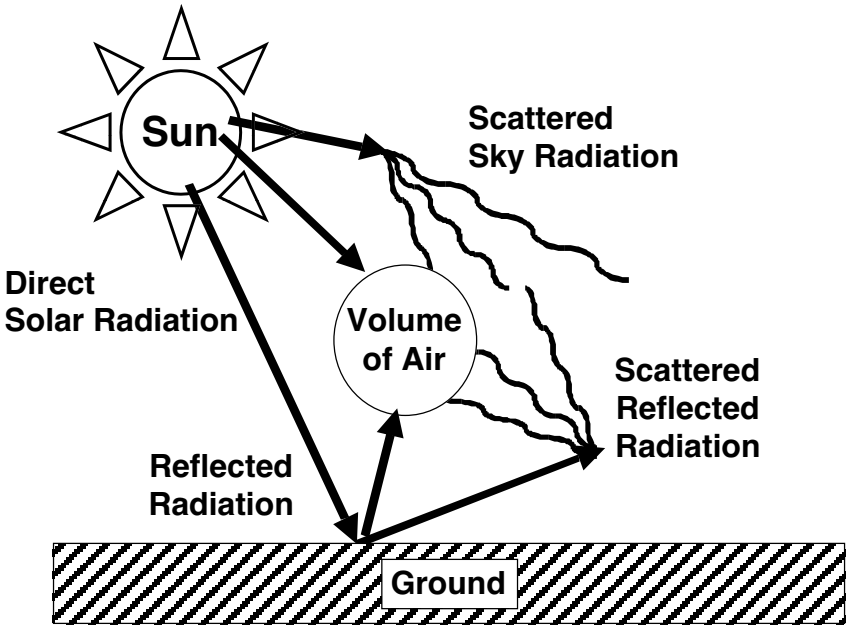

2. Setup of Spectral-Radiometers at Measurement Sites

The spectral-radiometers were obtained from Metcon Inc. and Dr. Rainer Schmitt of Metcon provided the initial training and laboratory setup of the instruments. Each spectral-radiometers consisted of a hemispherical radiation collection head, Figure 2-1, and a monolithic monochromator with a 512 pixel diode array detector. Overall the system had a spatial resolution of about 0.85 nm. The spectral-radiometers had an extremely fast response time, the radiation bands affecting the photolysis rate of nitrogen dioxide could be sampled at frequencies up to 5 Hz.

The spectral-radiometers were unpacked, setup and calibrated in the laboratory. The calibrations were performed with a 1000w calibration lamp as discussed under Section 3 of this report. The diode array spectrometers were calibrated in the laboratory before being placed in the field. The diode array spectrometers and supporting PCs were transported to the sites and mounted on the observation towers.

The spectral-radiometers were located at the University of California (UC-Davis); Sunol; CA; and the Desert Research Institute (DRI) in Reno, NV, Figure 2-2 and Figure 2-3. The instrument at UC-Davis provided actinic flux that is probably more representative of the overall CCOS domain and the instrument was co-located with a station of the U.S. Department of Agriculture - UVB Radiation Monitoring Program. The Sunol site was located at the CCOS-supersite and provided actinic flux taken near the Pacific coast. The instrument located at DRI provided data that was typical of the Sierra Mountains. The spectral-radiometer at UC-Davis operated from July 14, 11:00 am to October 25, 2000, 10:00 am; at Sunol the spectral-radiometer operated from July 19, 3:00 pm to September 22, 12:00, 2000; and the third operated at DRI from August 29, 6:00 pm to November 14, 8:00 pm, 2000.

Spectral averaging times on 0.5, 1, 2 and 5 seconds were used and a background was automatically subtracted from the spectra based on the number of counts of first few diodes in the field. The spectra were stored to the PC hard drive and the data was transferred to CD disks at regular intervals. For all calculations performed to calculate the photolysis rate parameters the data taken at 0.5 s were used because the full spectrum from 290 to 700 nm was available without any losses due to detector saturation.

Following the intensive CCOS field measurement period the spectrometer at Sunol was removed and taken to UC-Davis to determine the albedo correction function and to intercompare the two instruments. At UC-Davis both spectrometers were compared by taking a few hours of duplicate measurements on September 27, 2000, a clear day. Following that comparison the instrument moved from Sunol was turned 180° to face the ground. Almost one more month of data was obtained with the head of the diode array spectrometer from Sunol facing down while the UC-Davis instrument continued to collect data facing up. This data was used to correct the actinic flux data taken at Sunol

and to estimate the effect of albedo on the photolytic rate parameters, Figure 2-3, "4π Experiment" as discussed in Section 5.

Figure 2-1. Spectral-radiometer solar radiation collection head.

Figure 2-2. Locations of actinic flux measurement sites.

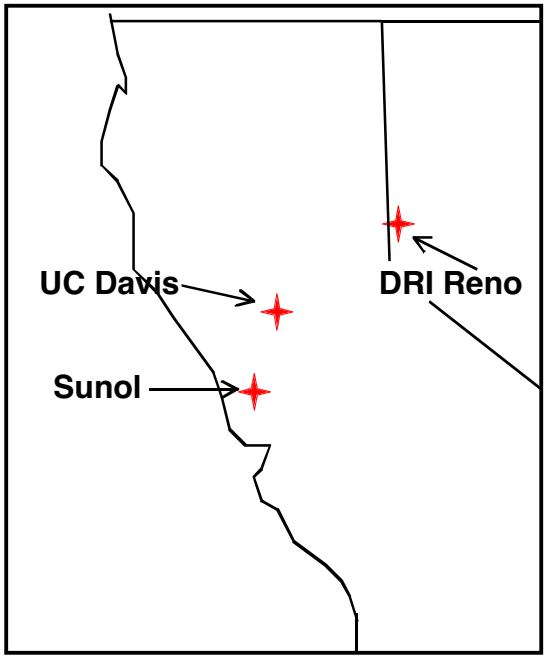

Figure 2-3. Setup of the spectral-radiometer at University of California at Davis, Sunol and DRI. The arrow at DRI points to the spectral-radiometer location.

3. Calibration of Spectral-Radiometers

The laboratory calibrations were made using the setup shown in Figure 3-1. A standard 1000w calibration lamp (NIST traceable) was placed 49.5 cm from the hemispheric sampling head. The calibration lamp should have been placed 50 cm from the head and therefore the known calibration spectrum was adjusted by a factor of $(50/49.5)^2$. The lamp required a specified current (8.000 A) and voltage (107.71 V) to provide a known calibration spectrum, Figure 3-2; this was accomplished with a regulated power supply. The light from the lamp passed through an aperture plate attached to a back plate that was attached to the sampling head. A black cloth covered the gap between the two plates to prevent stray light from reaching the head.

Figure 3-1. Calibration setup for spectral-radiometers.

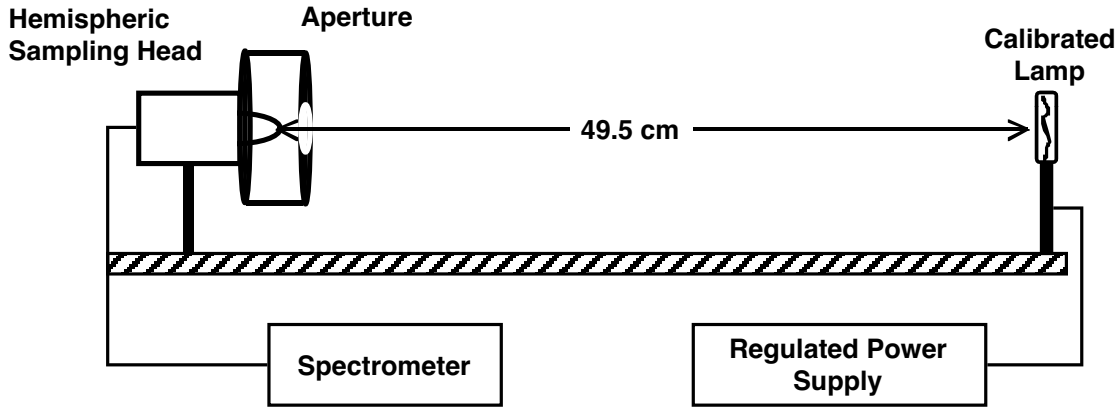

Figure 3-2. Irradiance spectrum of the standard calibration lamp.

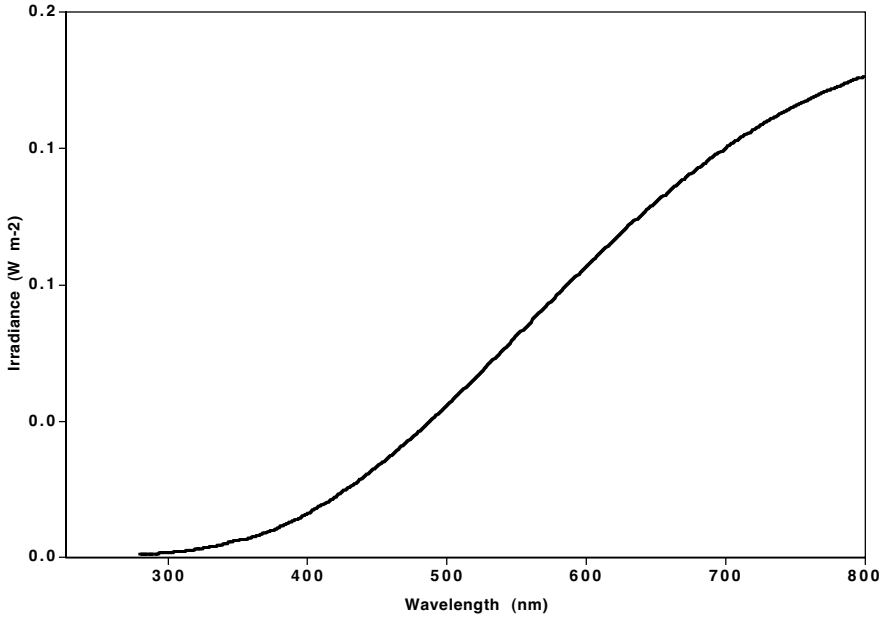

All three spectral-radiometers were calibrated several times to provide a measure of the reproducibility of the calibration curves. First the aperture was covered and five dark background counts were collected. Second a cutoff filter that passed radiation only above 325 nm was mounted on the aperture and five more spectra were collected. The purpose of the measurement with the cutoff filter was to evaluate stray light below 325 nm. However the stray light was found to be much less that the noise at these wavelengths and therefore this measurement was ignored in subsequent work. Finally five spectra were collected with the aperture fully open to the light beam. Calibration spectra were calculated by subtracting the background spectra from the full light spectra. For each spectral-radiometer multiple calibration spectra were averaged to produce the final calibration spectrum, Figure 3-3.

Figure 3-3. Original average calibration spectra produced by calibration procedure.

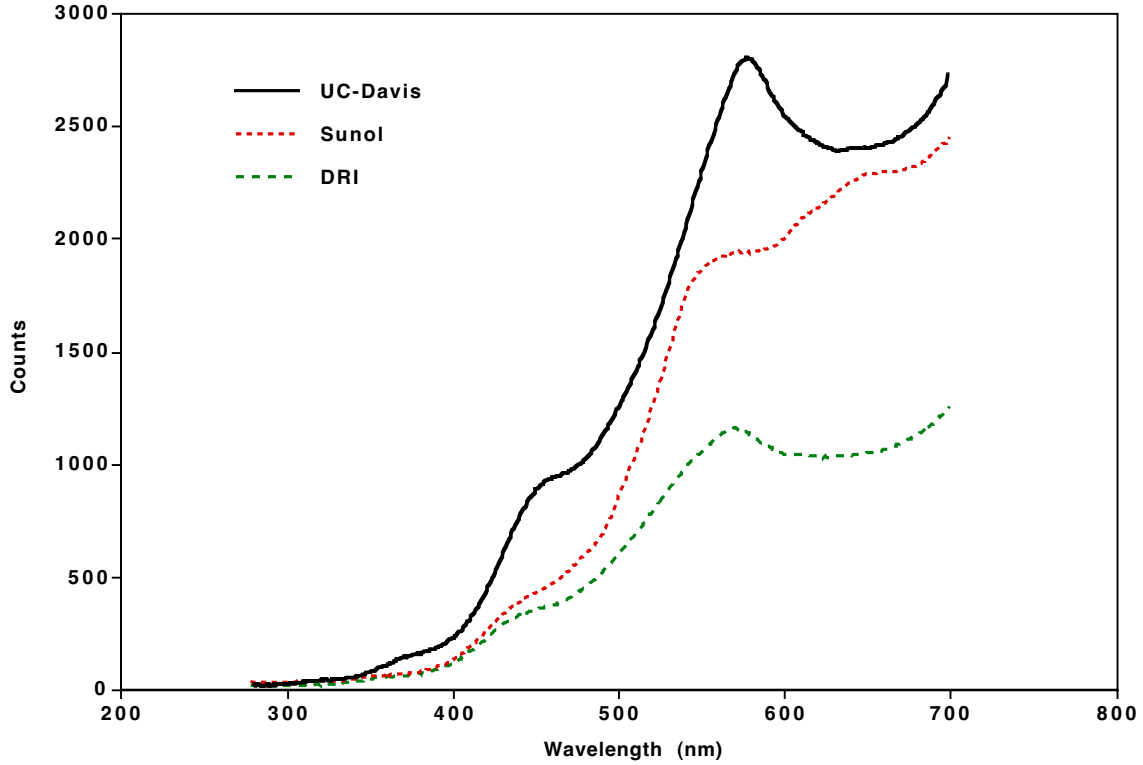

Actinic flux was calculated as described in Section 4. The actinic flux obtained from the spectral-radiometer placed at Sunol showed considerable curvature compared to the UC-Davis and DRI sites if the laboratory calibrations were used, Figure 3-4. The radiative program of Madronich (Madronich, 1987; Joseph et al., 1976) was modified to produce the downward welling hemispherically integrated flux and curvature in the measurements was not in accord with the simulation, Figure 3-5. Given the curvature in the Sunol data (despite repeated calibrations) the data from both instruments were used to reconcile the Sunol instrument measurements to the UC-Davis data.

Figure 3-4. Actinic flux at Noon Aug 31, 2000 with original calibration used for Sunol data.

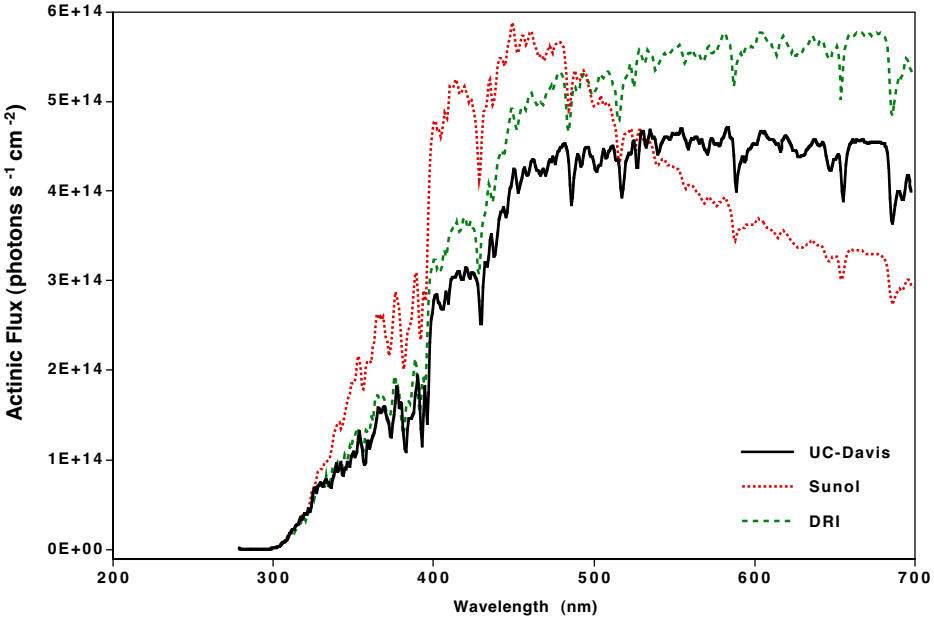

Figure 3-5. Actinic flux for a hemispheres sampling head calculated with Madronich radiative transfer model.

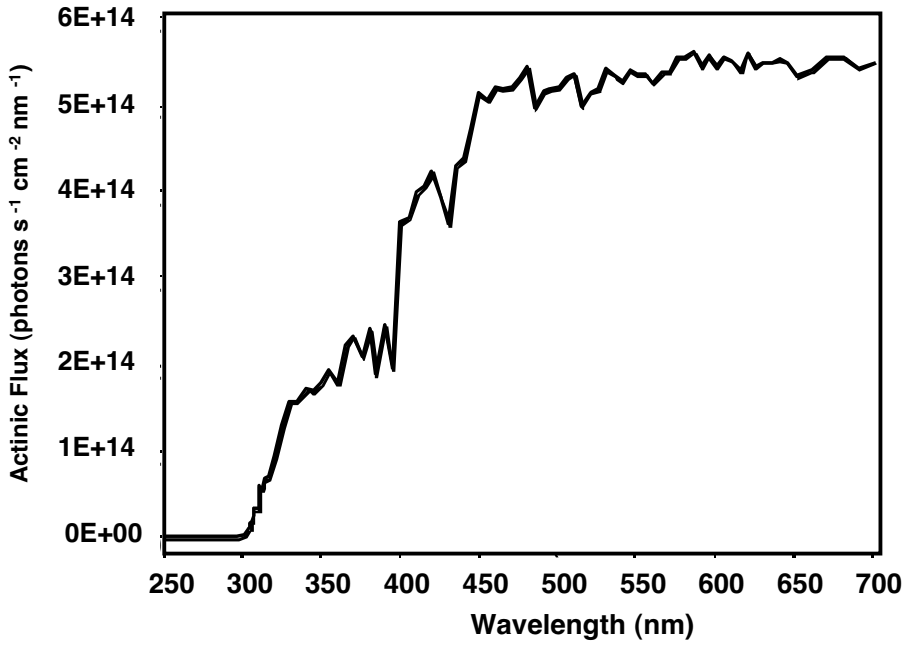

Both spectral-radiometers used to make measurements at Sunol and the spectral-radiometer at UC-Davis were placed in the vertical direction for a few hours near noon on September 27, 2000, a clear day, to determine a relative instrument response function to be used to account for the difference in response between the two instruments, Figure 3-6. A revised calibration function for the Sunol instrument was developed and used in the calculation of the photolysis rate parameters for Sunol, equation 3-1,

$$c_{Sunol\,Rev} = \frac{\phi_{Sunol@Davis\_up}}{\phi_{UC-Davis\_up}} \times c_{Davis} \qquad (3\text{-}1)$$

where $\phi_{Sunol@Davis\_up}$ and $\phi_{UC-Davis\_up}$ are the measured photon counts from the spectral-radiometers at UC-Davis and the instrument from Sunol (at UC-Davis), respectively, and c_{Davis} is the calibrated spectrum of the UC-Davis instrument. The revised calibration, Figure 3-7, reconciled the Sunol measurements with the UC-Davis measurements, Figure 3-8, and the revised calibration was applied to the Sunol data for the calculation of photolysis rate parameters.

Figure 3-6. Sunol instrument was moved to UC Davis site and both instruments were compared; plot for 09/27/2000, 12:44:08 pm.

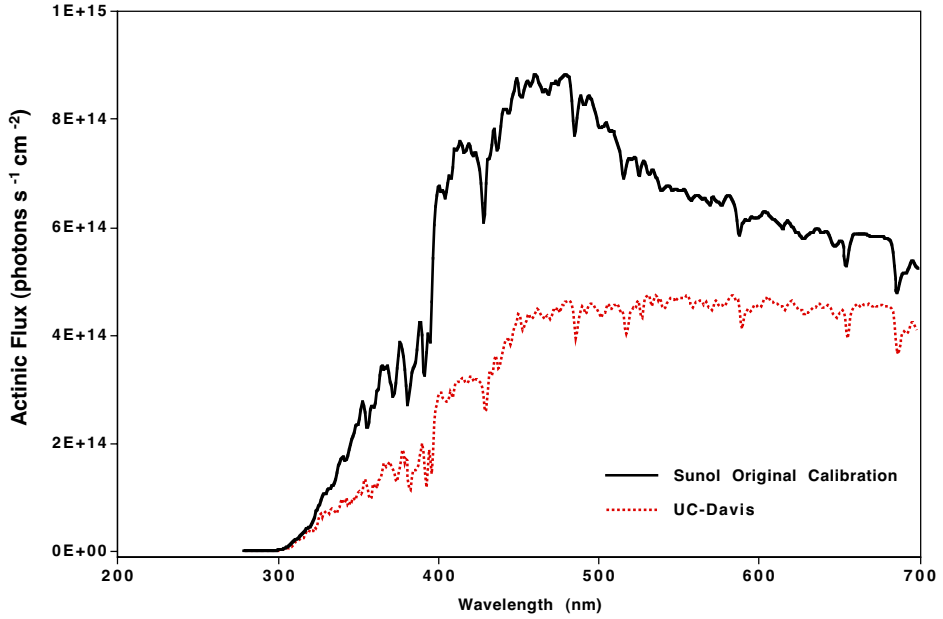

Figure 3-7. Sunol revised calibration based on intercomparison with instrument at UC-Davis.

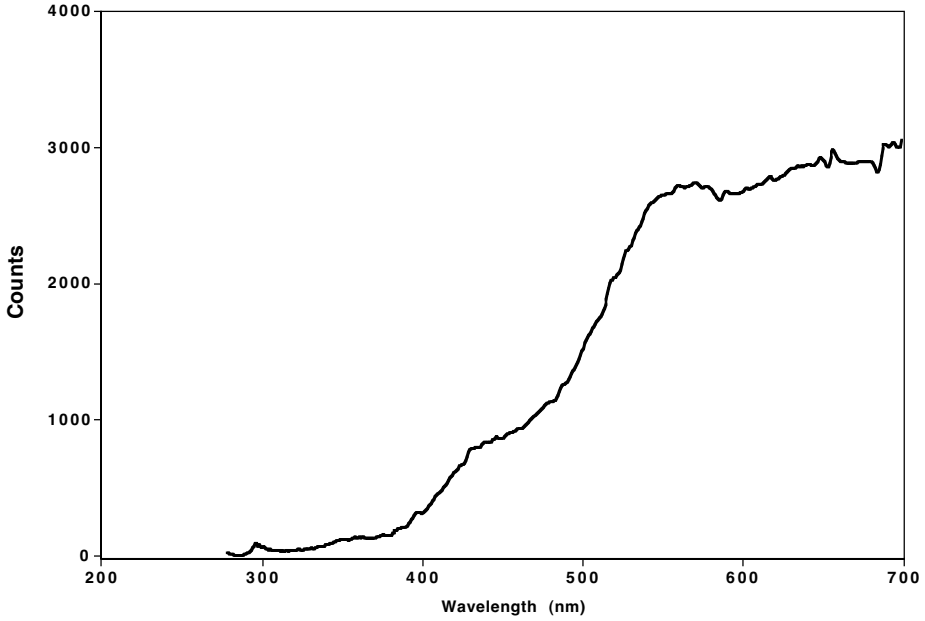

Figure 3-8. Sunol instrument was recalibrated to match UC-Davis instrument; plot for 09/27/2000, 12:44:08 pm. The solid black line represents the recalibrated Sunol spectral-radiometer data and the crossed red line represents the UC-Davis spectral-radiometer data.

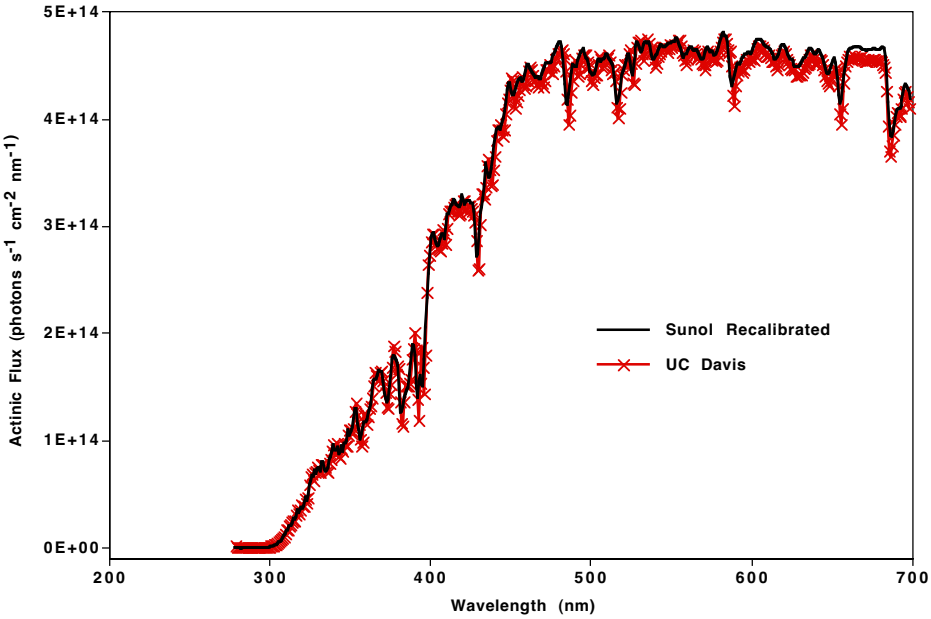

4. Calculation of 2π Actinic Flux from Spectral-Radiometer Measurements

The photon energy integrated over a hemisphere in W m^{-2} s^{-1} was calculated from equation 4-1.

$$\phi_w = \left\{ \frac{[m_i - b_i]}{c_i} \right\} \times I_i \qquad (4\text{-}1)$$

where ϕ_w is the actinic flux in photons s^{-1} cm^{-2} within a 1nm spectral interval, m_i is the number of counts measured by the spectral-radiometer, b_i is the background number of counts and c_i is the number of counts of the calibration spectrum.

To calculate photolysis rate parameters the actinic flux in W m^{-2} s^{-1} was converted to the flux of photons in photons s^{-1} cm^{-2} nm^{-1}. The energy of a single photon E is given by equation 4-2.

$$E = \frac{hc}{\lambda} \qquad (4\text{-}2)$$

where h is Planck's constant, c is the speed of light and λ is the photon's wavelength. The total number of photons in a wavelength interval, ϕ_p, is calculated by dividing the integrated photon energy by the average energy of a single photon in the interval as given by equation 4-3.

$$\phi_p = \frac{\phi_w}{hc} \lambda_{avg} \qquad (4\text{-}3)$$

where λ_{avg} is the wavelength of the photon with the average energy, equation 4-4.

$$\lambda_{avg} = \left(\frac{\lambda_1 + \lambda_2}{\lambda_1 \lambda_2} \right) \qquad (4\text{-}4)$$

where λ_1 and λ_2 are the first and last wavelengths of the wavelength interval. Neglect of using λ_{avg} and using the initial wavelength of the interval results in an error in of less than 0.2% in the calculated number of photons in the wavelength range between 300 and 700 nm given the 1 nm spacing of the spectral intervals. Adjusting the units so that ϕ_p is in photons s^{-1} cm^{-2} equation 4-3 becomes equation 4-5.

$$\phi_p\left(photons \;\; s^{-1} \;\; cm^{-2} \right) = \frac{\phi_w\left(J \;\; s^{-1} \;\; m^{-2} \right)}{h\left(J \;\; s \right) c\left(m \;\; s^{-1} \right)} \lambda_{avg}(nm) \frac{10^{-9} m}{1nm} \frac{1m^2}{10^4 cm^2} \qquad (4\text{-}5)$$

Taking the values of h as $6.6260755 \times 10^{-34}$ J s, c as 2.99792458×10^{8} m s^{-1} and collecting the unit correction factors, the actinic flux in photons s^{-1} cm^{-2} is related to the integrated photon energy by equation 4-6,

$$\phi_i = \phi_w \times 5.03411 \times 10^{11} \times \lambda_i \qquad (4\text{-}6)$$

where the constant, $5.0341125 \times 10^{+11}$, has the units of photons m^2 W^{-1} nm^{-1} cm^{-2}.

Finally combining equation 4-1 and 4-6 results in equation 4-7 that was used to calculate the actinic flux from the data.

$$\phi_i = \left\{ \frac{[s_i - b_i]}{c_i} \right\} \times I_i \times 5.03411 \times 10^{11} \times \lambda_i \qquad (4\text{-}7)$$

where ϕ_i is the actinic flux integrated over a hemisphere in photons s^{-1} cm^{-2} within a 1 nm spectral interval, m_i is the number of counts measured by the spectral-radiometer, b_i is the background number of counts, c_i is the number of counts for the calibration spectrum, I_i is the irradiance of the calibrated lamp in W m^{-2} s^{-1}, $5.0341125 \times 10^{+11}$ photons m^2 W^{-1} nm^{-1} cm^{-2} is the conversion factor and λ_i is the wavelength of the interval in nm.

Plots of the downward-welling actinic in photons s^{-1} cm^{-2} with the plotted spectral interval equal to1 nm are shown in Figures 4-1 and 4-2. The episodes July 30 to August 2 and September 17 to 21 corresponded to high ozone periods observed under CCOS. The actinic flux was reduced at UC-Davis on August 1 while at Sunol the noontime actinic flux was reduced on July 31 and was much lower on August 1. During the September episode the actinic flux was much more consistent and constant across the domain.

The actinic flux calculated in this section represents only the downward-welling component of the flux. To calculate photolysis rate parameters it is necessary to estimate the upward-welling of the actinic flux and as discussed in Section 5.

Figure 4-1. Hemispheric actinic flux measured at noon from the Sunol and UC-Davis sites for July 30 to August 2 given per 1 nm spectral intervals.

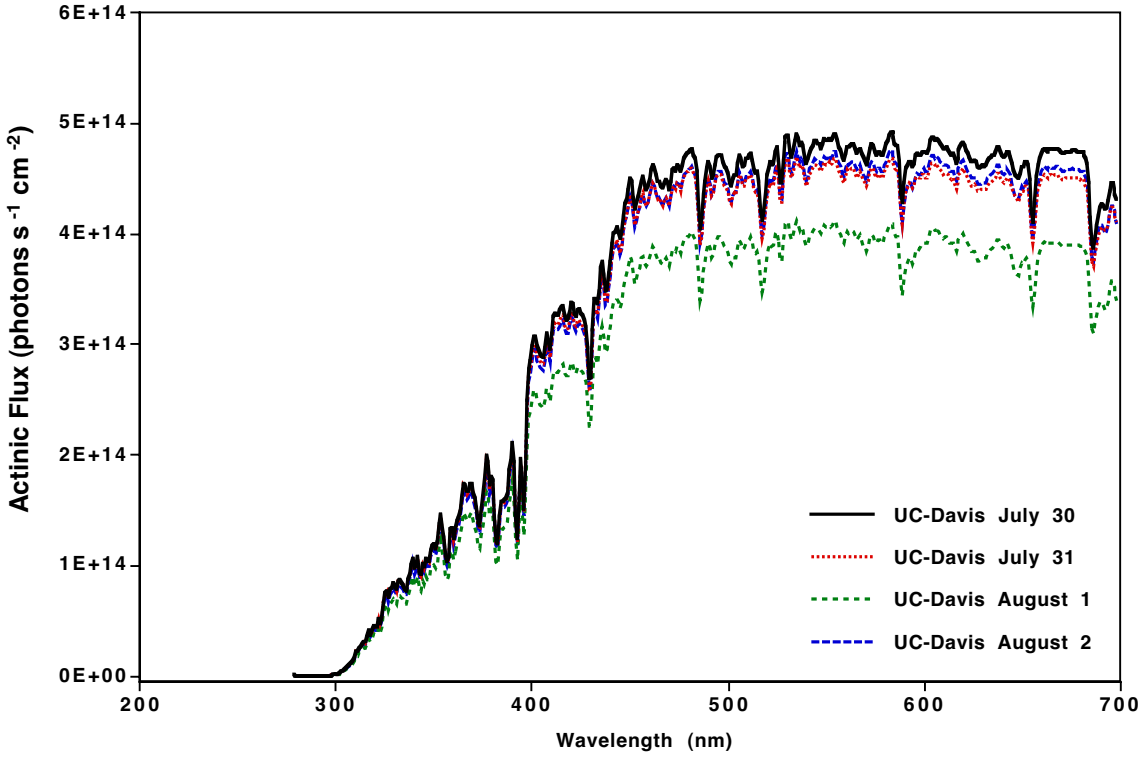

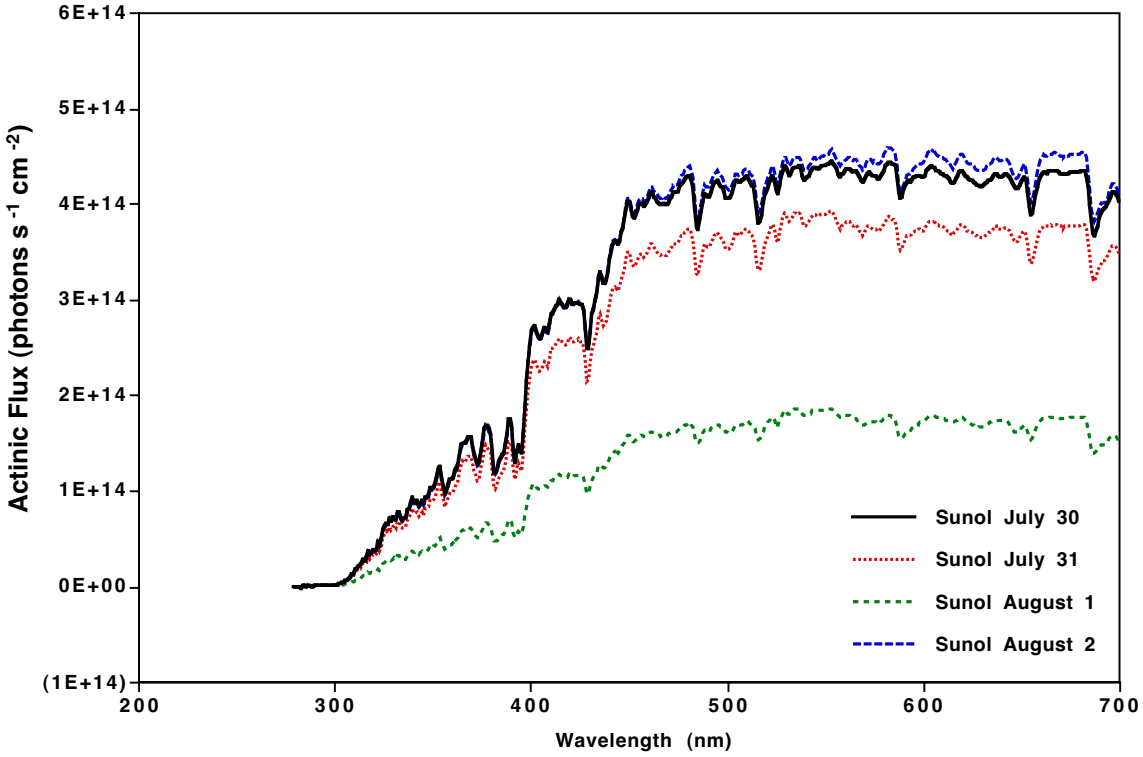

Figure 4-2. Hemispheric actinic flux measured at noon from all three sites for September 17 to 21 given per 1 nm spectral intervals.

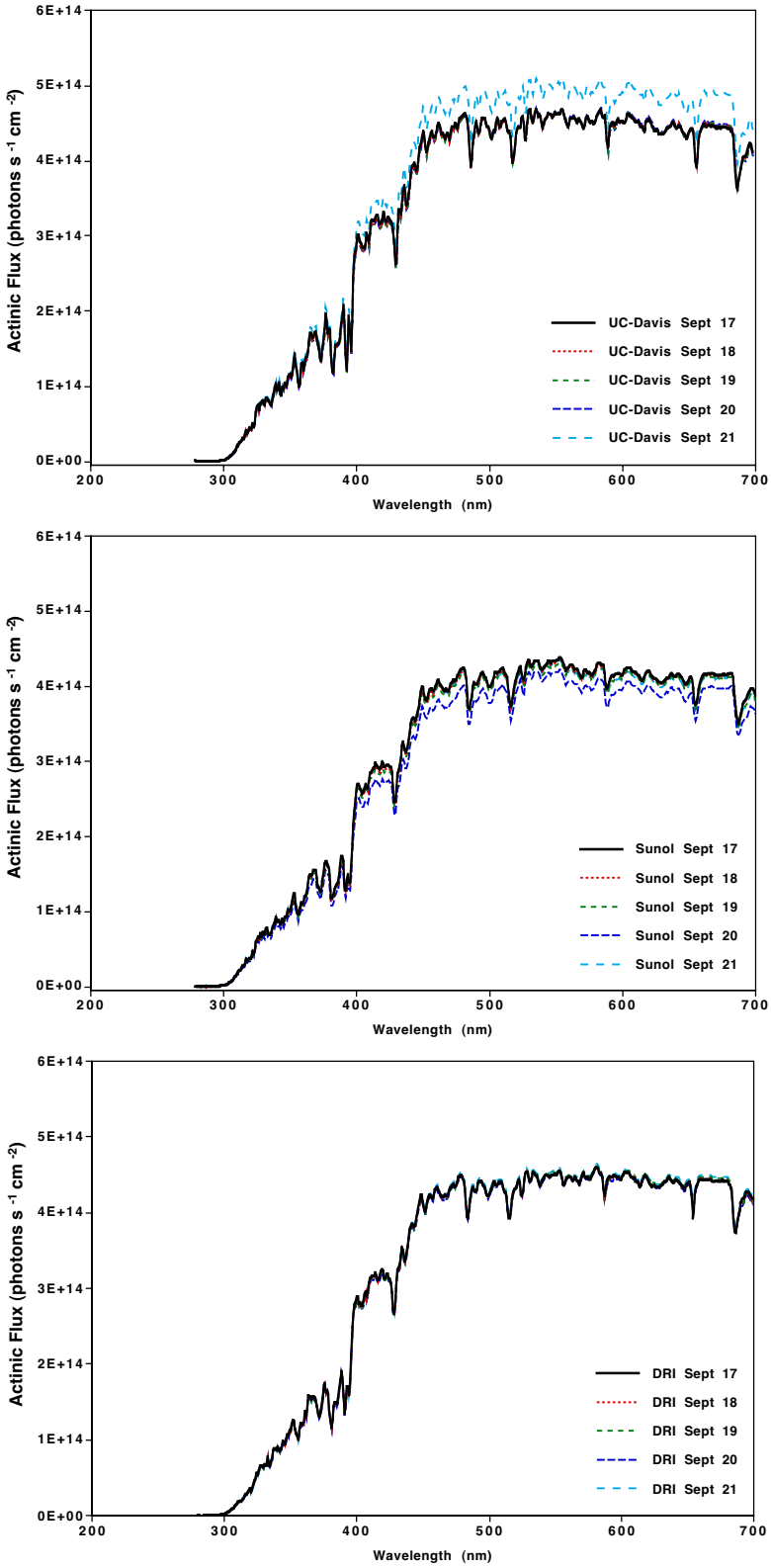

5. Determination of Albedo Correction Function

In the atmosphere actinic flux is defined as the flux of photons integrated over an infinitesimal sphere, and is often referred as a 4π integration. The radiation collectors used for the actinic flux measurements integrated photon flux with hemispherical collectors that integrated photons over 2π. However for almost a month at UC-Davis, two spectral-radiometers were operated with one spectral-radiometer pointing up and another spectrometer pointing down to collect radiation over 4π. The radiation measurements from the two spectral-radiometers were used to develop wavelength correction factors that were used to estimate the 4π actinic flux from the 2π measurements. The derivation is as follows.

Two spectrometers were used at UC-Davis. The spectral-radiometer labeled here as UC-Davis was placed continuously at UC-Davis while spectral-radiometer labeled here as Sunol@Davis was used to make measurements at Sunol and then moved to UC-Davis to develop a function to estimate 4π actinic flux from the 2π measurements. First both spectral-radiometers were placed in the vertical direction for a few hours near noon on September 27, a clear day, to determine a relative instrument response function to be used to account for the difference in response between the two instruments. Then a month's duration of measurements were collected with the spectral-radiometer from Sunol turned toward the ground. Spectra collected with 0.5 s averaging times were used in this analysis. The sum of the two spectral-radiometer measurements (with the correction for differences in the response function between the two instruments) represents a 4π measurement. However, the actinic flux can be expressed as a correction function applied to the upward looking measurement only as shown below.

If ϕ_{Sunol_up} and $\phi_{UC-Davis\_up}$ are the measured photon counts from spectral-radiometers then the ratio of the response of the two spectral-radiometers is given by:

$$C = \frac{\phi_{UC-Davis\_up}}{\phi_{Sunol@Davis\_up}} \tag{5-1}$$

The ratio of the spectral-radiometer measurements between 290 and 695.5 nm was calculated for September, 27 between the times 12:36:02 and 13:15:05. During this time period 40 measurements were collected and these were ratioed according to equation 5-1 and averaged to produce the values plotted in Figure 5-1. The percent standard deviations from the mean are plotted in Figure 5-2. For wavelengths greater than 302 nm the standard deviations are between ~3 to 4 %.

Figure 5-1. Ratio of photon counts measured by spectral-radiometer at UC-Davis to those measured by spectral-radiometer Sunol@Davis.

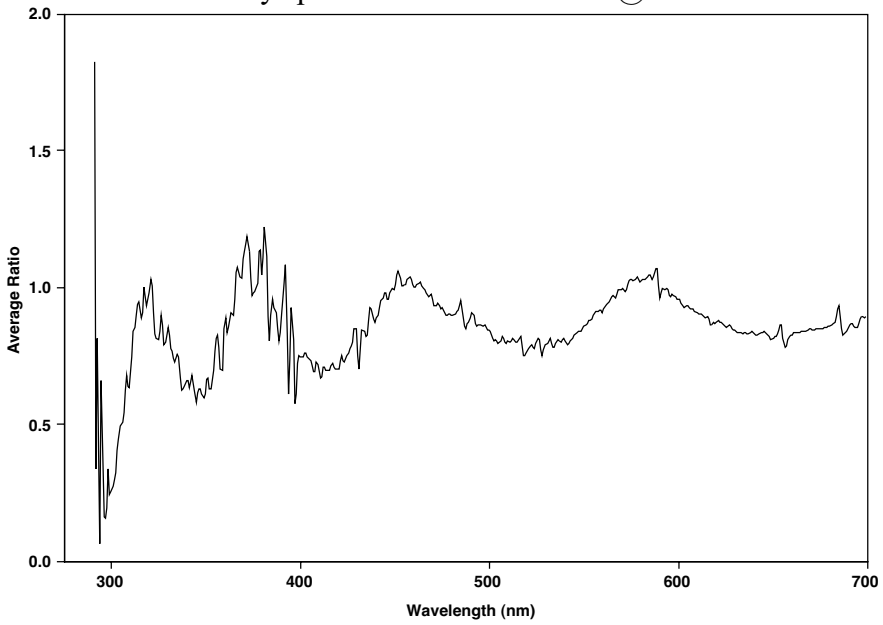

Figure 5-2. Standard deviation of ratio of photon counts measured by spectral-radiometer at UC-Davis to those measured by spectral-radiometer Sunol@Davis expressed as a percent.

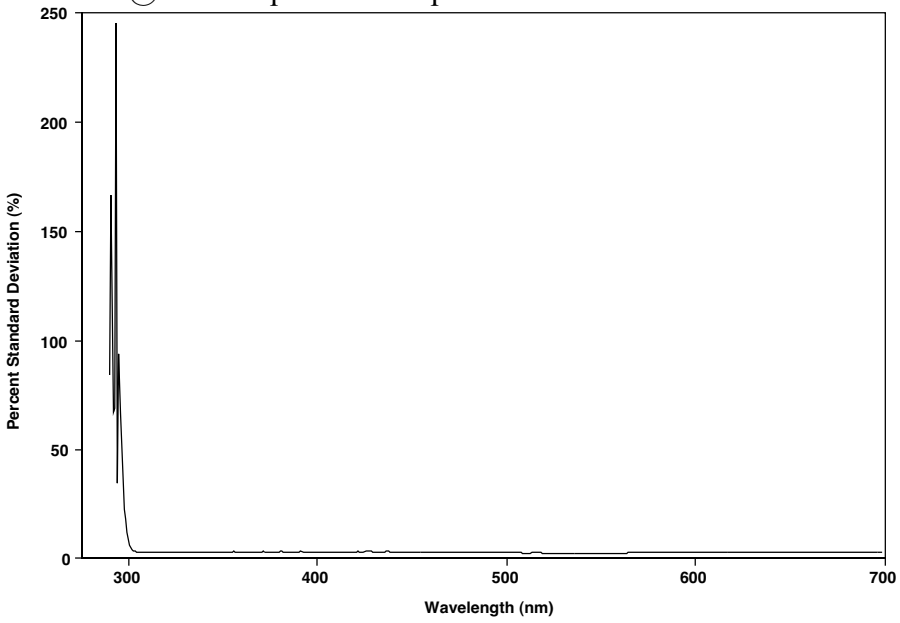

Following this experiment the spectral-radiometer Sunol@Davis was placed facing the ground to measure the upward welling radiation $\phi_{Sunol@Davis\_down}$.

The spherically integrated number of photon counts made with the Sunol@Davis pointing down and UC-Davis pointing up is given by equation (5-2) (provided that the UC-Davis instrument is used as the reference instrument).

$$\phi_{total} = \phi_{UC-Davis\_up} + C\phi_{Sunol@Davis\_down} \tag{5-2}$$

Dividing both sides by $\phi_{UC-Davis\_up}$ yields equation (5-3) and rearranging (5-3) yields (5-4).

$$\frac{\phi_{total}}{\phi_{UC-Davis\_up}} = \frac{\phi_{UC-Davis\_up} + C\phi_{Sunol@Davisdown}}{\phi_{UC-Davis\_up}} \tag{5-3}$$

$$\phi_{total} = \phi_{UC-Davis\_up}\left[1 + C\frac{\phi_{Sunol@Davis\_down}}{\phi_{UC-Davis\_up}}\right] \tag{5-4}$$

The value of the correction function, $\left[1 + C\frac{\phi_{Sunol@Davis\_down}}{\phi_{UC-Davis\_up}}\right]$, was calculated for four clear days: September 28, October 5, October 12 and October 17. To determine the ratio $\frac{\phi_{Sunol@Davis\_down}}{\phi_{UC-Davis\_up}}$, the hourly average number of counts for the hours between 4:00 AM and 7:00 PM were calculated for both spectral-radiometers. These average values were ratioed, multiplied by the relative instrument response function and added to 1. However the values for times earlier than 8:00 AM and later than 4:00 PM were extremely noisy and were not used in the final average. The results for these four days are plotted in Figures 5-3 through 5-6.

Figure 5-3. Albedo correction function calculated for September 28, 2000.

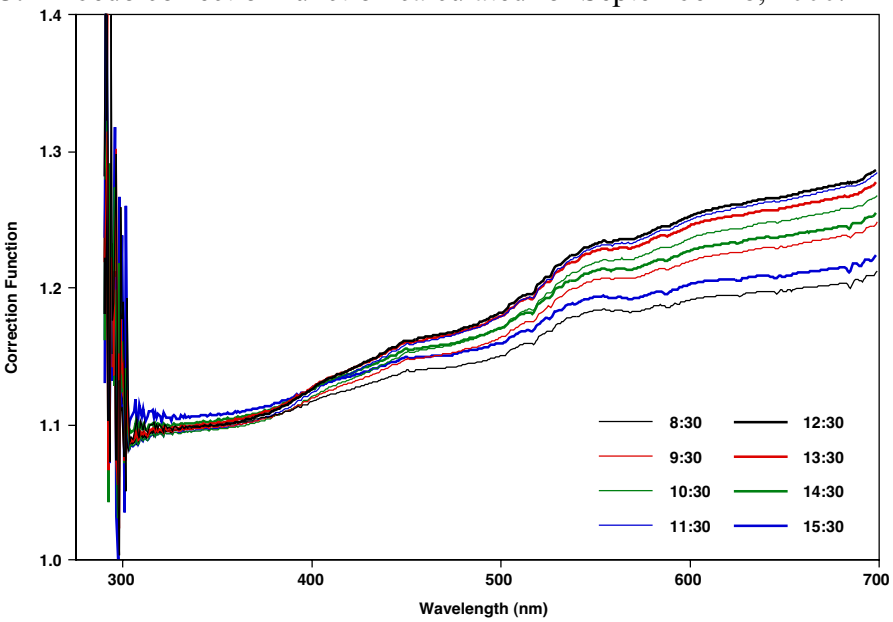

Figure 5-4. Albedo correction function calculated for October 5, 2000.

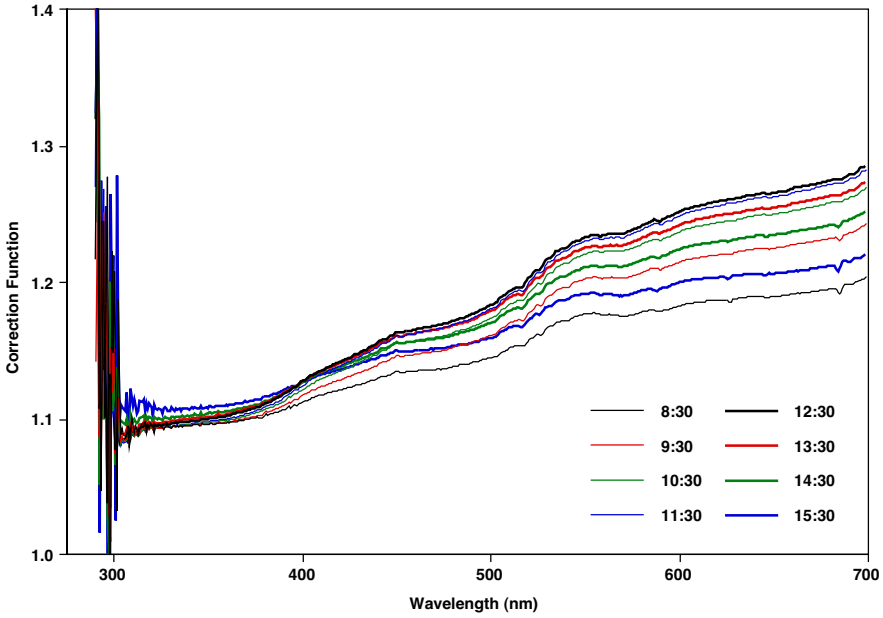

Figure 5-5. Albedo correction function calculated for October 12, 2000.

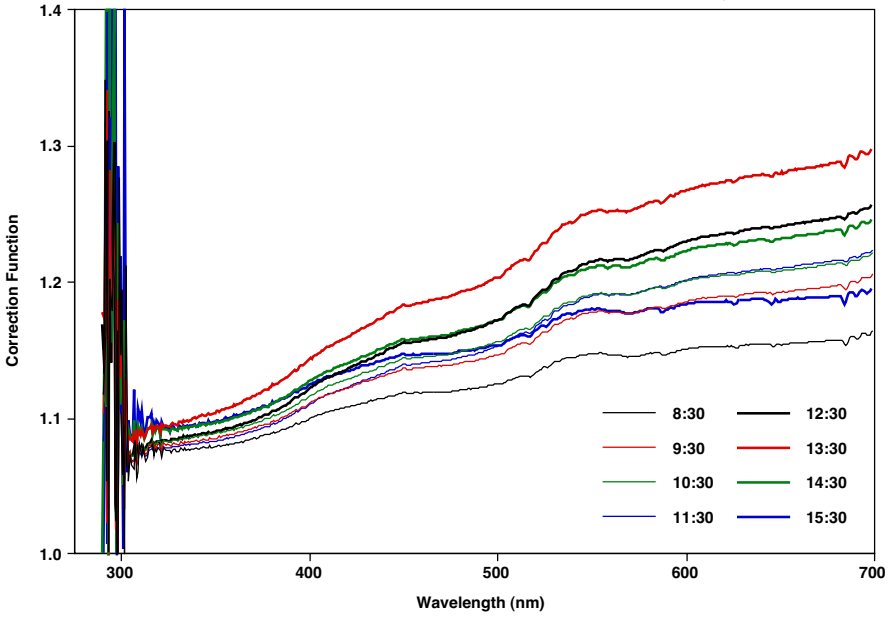

Figure 5-6. Total albedo correction function calculated for October 17, 2000.

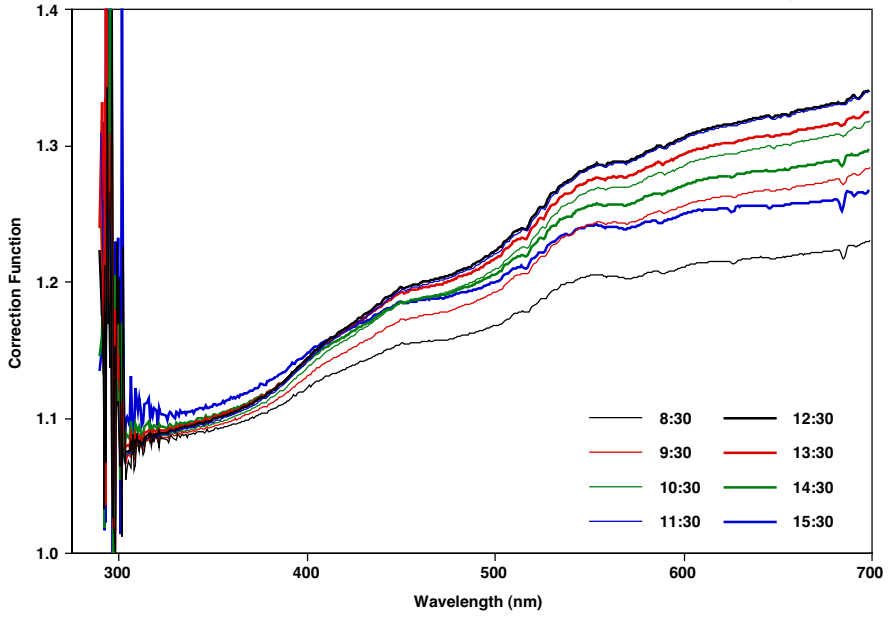

Figures 5-3 through 5-6 show that there is some variation in the albedo correction function with time of day. It tends to be higher during midday than during the early morning hours but there is also considerable variation between the values calculated at the same time for different days. The diurnal variation in the albedo correction function was ignored and the albedo correction functions for times between 8:00 AM and 4:00 PM were averaged. The average showed a low standard deviation in spite of the variation, Figures 5-7 and 5-8. The average was smoothed and this was used as the final correction function, Figure 5-9.

Figure 5-7. Average albedo correction function.

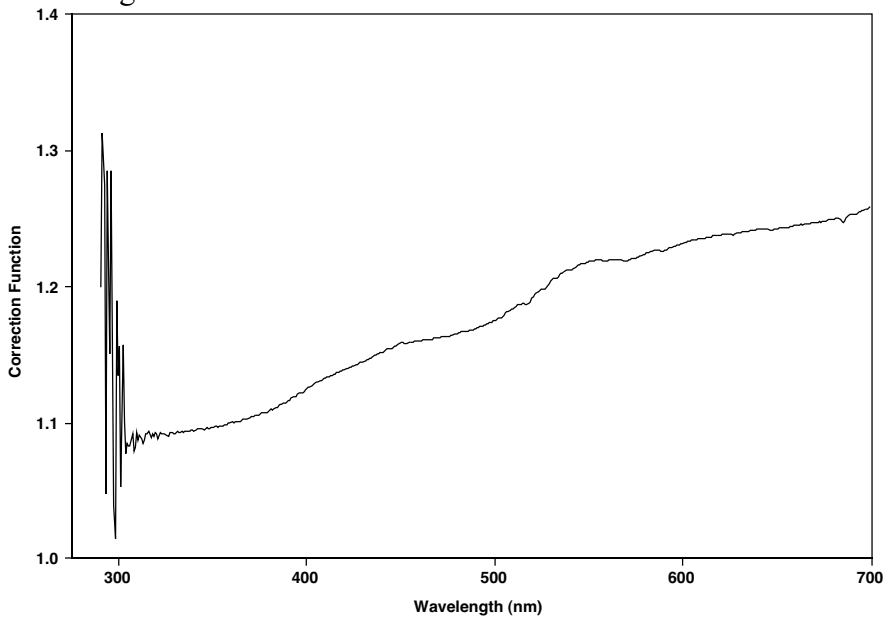

Figure 5-8. Standard deviation of albedo correction function expressed as a percent.

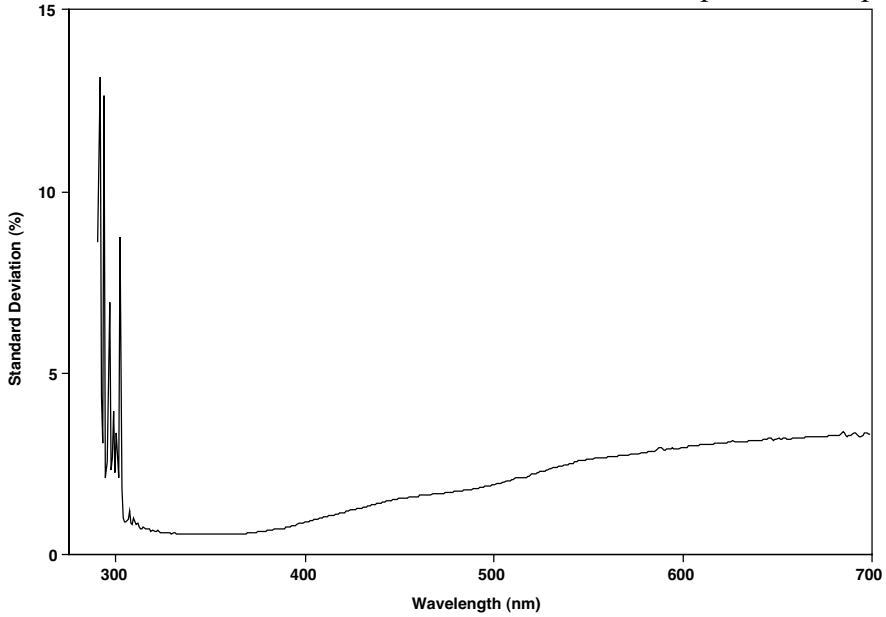

Figure 5-9. Smoothed average albedo correction function.

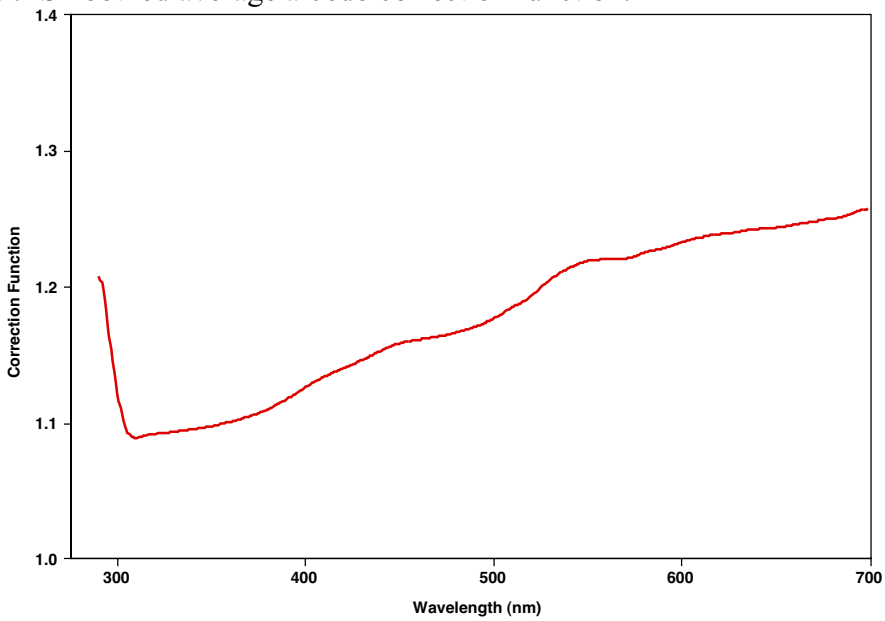

6. Calculation of Photolysis Rate Parameters from 4π Actinic Flux

The actinic flux measurements that were collected with a 0.5 s averaging time were used in this analysis because these were not saturated over the entire spectral range throughout the daylight hours. The hemispherical 2π flux (Section 4) was multiplied by the albedo correction function (Section 5) to calculate spherical 4π actinic flux. The photolysis rate parameters for the reactions given in Table 6-1 were calculated according to the following equation repeated here from Section 1 (Jacobson, 1999).

$$J = \sum I(\lambda) \times \sigma(\lambda) \times \phi(\lambda) \times \Delta\lambda \qquad (1\text{-}1)$$

Table 6-1 also lists the cross sections and quantum yields used in the calculations. The albedo correction function, standard lamp irradiances and absorption cross-sections and quantum yields were interpolated to the wavelength grid for each spectrometer to permit the photolysis rate parameters to be calculated.

Table 6-1. Sources of cross sections and quantum yields used[a].

Reaction	Cross Sections	Quantum Yields
$NO_2 + h\nu \rightarrow NO + (O^3P)$	DeMore et al. (1997)	DeMore et al. (1997)
$O_3 + h\nu \rightarrow O_2 + O(^1D)$	Molina and Molina (1986)	Sander et al. (2000)
HCHO + hν → H_2 + CO "Molecular Reaction"	Wavelengths <300 nm: Moortgat et al. [1980]; Wavelengths >300 nm: Cantrell et al. [1990]	Wavelengths <300nm: Atkinson et al. (1994); Wavelengths >300nm DeMore et al. (1994)
HCHO + hν (+O_2) → 2 HO_2 + CO "Radical Reaction"	Wavelengths <300 nm: Moortgat et al. (1980); Wavelengths >300 nm: Cantrell et al. (1990)	Wavelengths <300nm: Atkinson et al. (1994); Wavelengths >300nm DeMore et al. (1994)

[a]300 K and 1 atmosphere were assumed.

Tables 6-2 and 6-3 list average absorption cross sections and quantum yields of NO_2, Tables 6-4 and 6-5 list average absorption cross sections and quantum yields of O_3, Tables 6-6 lists average absorption cross sections of HCHO and Tables 6-7 and 6-8 list the quantum yields of the molecular and radical reactions of HCHO, respectively. The measured photolysis rate parameters and a comparison with simulated values are discussed in Section 7.

Table 6-2. Average absorption cross sections of NO_2 used in this work.

Wavelength (nm)	NO_2 Cross Section (cm^2)	Wavelength (nm)	NO_2 Cross Section (cm^2)	Wavelength (nm)	NO_2 Cross Section (cm^2)
273.97-277.78	5.05E-20	322.50-327.50	2.78E-19	377.50-382.50	5.62E-19
277.78-281.69	5.90E-20	327.50-332.50	3.10E-19	382.50-387.50	5.73E-19
281.69-285.71	6.99E-20	332.50-337.50	3.39E-19	387.50-392.50	5.90E-19
285.71-289.85	8.14E-20	337.50-342.50	3.76E-19	392.50-397.50	5.83E-19
289.85-294.12	9.71E-20	342.50-347.50	4.02E-19	397.50-402.50	6.01E-19
294.12-298.51	1.15E-19	347.50-352.50	4.28E-19	402.50-407.50	5.77E-19
298.51-303.03	1.34E-19	352.50-357.50	4.67E-19	407.50-412.50	5.97E-19
303.03-307.69	1.58E-19	357.50-362.50	4.81E-19	412.50-417.50	5.65E-19
307.69-312.50	1.85E-19	362.50-367.50	5.13E-19	417.50-422.50	5.78E-19
312.50-317.50	2.14E-19	367.50-372.50	5.29E-19		
317.50-322.50	2.46E-19	372.50-377.50	5.49E-19		

Table 6-3. Average quantum yields of NO_2 used in this work.

Wavelength (nm)	NO_2 Quantum Yield	Wavelength (nm)	NO_2 Quantum Yield	Wavelength (nm)	NO_2 Quantum Yield
280-285	1.000	382-383	0.973	403-404	0.485
285-295	0.999	383-384	0.972	404-405	0.425
295-300	0.998	384-385	0.971	405-406	0.350
300-305	0.997	385-386	0.969	406-407	0.290
305-310	0.996	386-387	0.967	407-408	0.225
310-315	0.995	387-388	0.966	408-409	0.185
315-320	0.994	388-389	0.964	409-410	0.153
320-325	0.993	389390	0.962	410-411	0.130
325-330	0.992	390-391	0.960	411-412	0.110
330-335	0.991	391-391	0.959	412-413	0.094
335-340	0.990	392-393	0.957	413-414	0.083
340-345	0.989	393-394	0.953	414-415	0.070
345-350	0.988	394-395	0.950	415-416	0.059
350-355	0.987	395-396	0.942	416-417	0.048
355-360	0.986	396-397	0.922	417-418	0.039
360-365	0.984	397-398	0.870	418-419	0.030
365-370	0.983	398-399	0.820	419-420	0.023
370-375	0.981	399-400	0.760	420-421	0.018
375-380	0.979	400-401	0.695	421-422	0.012
380-381	0.975	401-402	0.635	422-423	0.008
381-382	0.974	402-403	0.560	423-424	0.004
				424-700	0.000

Table 6-4. Average absorption cross sections of O_3 used in this work.

Wavelength (nm)	O_3 Cross Section (cm^2)	Wavelength (nm)	O_3 Cross Section (cm^2)
277.78-281.69	4.06E-18	312.50-317.50	4.55E-20
281.69-285.14	2.82E-18	317.50-322.50	2.20E-20
285.14-289.86	1.78E-18	322.50-327.50	1.00E-20
289.86-294.12	1.07E-18	327.50-332.50	5.00E-21
294.12-298.51	6.06E-19	332.50-337.50	2.12E-21
298.51-303.03	3.31E-19	337.50-342.50	8.18E-22
303.03-307.70	1.75E-19	342.50-347.50	4.35E-22
307.70-312.50	9.12E-20	347.50-700.00	0.00E+00

Table 6-5. Average quantum yields of O_3 used in this work.

Wavelength (nm)	O_3 Quantum Yield	Wavelength (nm)	O_3 Quantum Yield
300-301	0.9489	318-319	0.1993
301-302	0.9558	319-320	0.1777
302-303	0.9613	320-321	0.1560
303-304	0.9684	321-322	0.1354
304-305	0.9750	322-323	0.1171
305-306	0.9733	323-324	0.1017
306-307	0.9511	324-325	0.0894
307-308	0.8949	325-326	0.0800
308-309	0.7962	326-327	0.0731
309-310	0.6610	327-328	0.0682
310-311	0.5133	328-329	0.0650
311-312	0.3869	329-330	0.0629
312-313	0.3053	330-335	0.0617
313-314	0.2672	335-445	0.0600
314-315	0.2536	445-450	0.0600
315-316	0.2458	450-4502	0.0600
316-317	0.2347	450.2-700	0.0000
317-318	0.2188		

Table 6-6. Average absorption cross section of HCHO used in this work.

Wavelength (nm)	NO_2 Cross-section (cm^2)	Wavelength (nm)	NO_2 Cross-section (cm^2)	Wavelength (nm)	NO_2 Cross-section (cm^2)
216-219	0.00E+00	262-265	5.84E-21	308-309	1.31E-20
219-221	2.93E-22	265-269	6.51E-21	309-310	3.10E-20
221-224	3.42E-22	269-272	1.02E-20	310-311	1.82E-20
224-226	1.02E-21	272-276	1.14E-20	311-312	5.96E-21
226-229	4.56E-22	276-280	1.76E-20	312-313	1.11E-20
229-231	5.27E-22	280-284	1.80E-20	313-314	9.11E-21
231-234	5.37E-22	284-288	2.59E-20	314-316	4.57E-20
234-237	3.47E-22	288-292	2.27E-20	316-320	4.23E-20
237-240	7.59E-22	292-296	2.75E-20	320-325	1.42E-20
240-243	6.28E-22	296-301	3.18E-20	325-330	2.43E-20
243-245	9.74E-22	301-303	1.60E-20	330-335	1.78E-20
245-249	1.04E-21	303-304	2.45E-20	335-340	1.29E-21
249-252	2.19E-21	304-305	6.37E-20	340-345	2.13E-20
252-255	2.28E-21	305-306	4.26E-20	345-350	6.61E-21
255-258	3.57E-21	306-307	3.99E-20	350-355	1.39E-21
258-262	3.74E-21	307-308	1.86E-20	355-360	8.27E-21
				360-700	0.00E+00

Table 6-7. Average quantum yield of HCHO + hν → H_2 + CO used in this work.

Wavelength (nm)	HCHO Quantum Yield	Wavelength (nm)	HCHO Quantum Yield	Wavelength (nm)	HCHO Quantum Yield
237-240	0.0000	284-288	0.3078	312-313	0.2690
240-243	0.4921	288-292	0.2946	313-314	0.2735
243-245	0.4837	292-296	0.2809	314-316	0.2789
245-249	0.4833	296-301	0.2669	316-320	0.3103
249-252	0.4875	301-303	0.2533	320-325	0.3941
252-255	0.4925	303-304	0.2490	325-330	0.5081
255-258	0.4955	304-305	0.2470	330-335	0.6761
258-262	0.4939	305-306	0.2456	335-340	0.7593
262-265	0.4855	306-307	0.2480	340-345	0.6361
265-269	0.4688	307-308	0.2510	345-350	0.5015
269-272	0.4434	308-309	0.2540	350-355	0.3734
272-276	0.4094	309-310	0.2570	355-360	0.2290
276-280	0.3684	310-311	0.2602	360-365	0.1036
280-284	0.3231	311-312	0.2645	365-370	0.0059
				370-700	0.0000

Table 6-8. Average quantum yield of HCHO + hν (+O_2) → 2 HO_2 + CO used in this work.

Wavelength (nm)	HCHO Quantum Yield	Wavelength (nm)	HCHO Quantum Yield
237-240	0.0000	303-304	0.7530
240-243	0.2641	304-305	0.7540
243-245	0.2889	305-306	0.7548
245-249	0.2970	306-307	0.7540
249-252	0.2951	307-308	0.7530
252-255	0.2894	308-309	0.7520
255-258	0.2855	309-310	0.7510
258-262	0.2881	310-311	0.7495
262-265	0.3010	311-312	0.7450
265-269	0.3268	312-313	0.7396
269-272	0.3668	313-314	0.7317
272-276	0.4205	314-316	0.7233
276-280	0.4860	316-320	0.6903
280-284	0.5591	320-325	0.5931
284-288	0.6339	325-330	0.4581
288-292	0.7021	330-335	0.3050
292-296	0.7335	335-340	0.1223
296-301	0.7408	340-345	0.0034
301-303	0.7478	345-700	0.0000

7. Comparison of Photolysis Rate Parameters with Model Values and Discussion of Results

An estimate of the uncertainty in the photolysis rate parameters as derived from the photolysis rate measurements can be derived by a propagation of errors analysis (Cvetanovic et al., 1975). Following Cvetanovic et al. the standard deviation of a photolysis rate parameter calculated from equation 1-1 is given by equation 7-1 where the symbols are defined as above and the standard deviation of J and each term is denoted by SD.

$$SD_J = \sum \Delta\lambda \times \left(\left(I(\lambda) \times \sigma(\lambda) \times SD_{\phi(\lambda)} \right)^2 + \left(I(\lambda) \times \phi(\lambda) \times SD_{\sigma(\lambda)} \right)^2 + \left(\sigma(\lambda) \times \phi(\lambda) \times SD_{I(\lambda)} \right)^2 \right)^{\frac{1}{2}} \quad (7\text{-}1)$$

The relative magnitude of the standard deviation can be estimated by assuming a few typical values for the actinic flux, the average absorption cross section and the average quantum yield in a single term of equation 7-1. If the magnitude of the actinic flux is 1×10^{-14} photons s^{-1} cm^{-2}, the quantum yield is 1 and the average absorption cross section is 1×10^{-20} cm^{-2} with uncertainties of 20, 20 and 10%, respectively, the uncertainty in the calculated photolysis rate parameter is ±30%. The uncertainties in the cross sections and quantum yields are typical of laboratory data. It seems conservative to assume a 10% uncertainty in the actinic flux based on calibration uncertainties and another 10% due to uncertainties in the albedo correction function.

The photolysis rate parameters and their ratios to the photolysis rate parameter of NO_2 (JNO_2) were compared with simulated values calculated by a radiative transfer model based on the delta-Eddington technique (Madronich, 1987; Joseph et al., 1976), Figures 7-1 to 7-28 and Tables 7-1 to 7-4. The comparisons were made for two CCOS episodes, July 30 to August 2, 2000 (July-August episode) and September 17 to 21, 2000 (September episode). The values of the ratios were not plotted for the nighttime hours.

The measured values of JNO_2 are shown in Figure 7-1 and the simulated values are shown in Figure 7-2 for the July-August episode. The shape of the JNO_2 measurements is similar to the simulation but August 1 appears to have been affected by clouds, especially at Sunol. There is a high frequency component in the Sunol data and occasionally seen in the UC-Davis data (July 30) that is probably electrical noise. The Sunol research site was located in a telecommunications building while the UC-Davis instrument was located in a structure remote from extensive communications activity.

JNO_2 is low at both sites relative to the simulation. The median of the four daily maximum values of the July-August episode are compared in Table 7-1 and the percent

differences (PD) between the measured (J_S) and simulated (J_S) values were calculated with the measurement serving as the reference value (equation 7-1).

$$PD = \left(\frac{J_S - J_M}{J_M} \right) \times 100\% \qquad (7\text{-}1)$$

During the July-August episode at the UC-Davis site the simulated maximum JNO_2 is 40% greater than the measured value while at the Sunol site the simulated maximum JNO_2 46% greater than the measurement.

The measured and simulated values of JNO_2 during the September episode are shown in Figure 7-3 and 7-4. The simulated maximum values of JNO_2 drop between the July-August episode by more than 10% from near 9×10^{-3} s^{-1} (0.54 min^{-1}) to about 8×10^{-3} s^{-1} (0.48 min^{-1}), Tables 7-1 and 7-3. The decrease in measured JNO_2 between the two episodes is much less at UC-Davis (2%) and Sunol (7%). However the decrease in simulated JNO_2 leads to better agreement between the simulation and measurements. The simulated JNO_2 is 21% higher at UC-Davis, 29% higher at Sunol and 24% higher at DRI.

The Sunol instrument remained affected by the high frequency signal but the UC-Davis and DRI instruments were relatively noise free. The UC-Davis was affected apparently by noise for a period on September 21 around noon and there is a daily spike in the DRI instrument that occurred during midmorning hours.

Measurements and simulations of the rate parameters for the photolysis of O_3 to produce O^1D (JO_3) are given in Figures 7-5 and 7-6 for the July-August episode. The photolysis rate parameter is much more dependent on the lower wavelengths of ultraviolet radiation; this affects the shape of the JO_3 time series, the seasonal change in values and the accuracy of the measurement. The shape of the time series of both the measured and simulated values are much narrower than the JNO_2 time series as expected (Finlayson-Pitts and Pitts, 1999). The agreement between the simulation and measured values is much worse for JO_3 than for JNO_2. The simulation is 139% higher at the UC-Davis site and 165% higher at the Sunol site, Table 7-1. This larger difference may be due to the lack of sensitivity and low signal to noise ratio of the diode array at wavelengths less than about 390 to 395 nm.

The difference between the simulated maximum of JO_3 for the July-August episode and the September episode is 28%, much greater than the change in JNO_2. The change between the JO_3 between the episodes in not seen in the measurement made at UC-Davis and Sunol, Figures 7-5 and 7-7. The measurements of JO_3 made at DRI are considerably higher than those made at the other two sites but this difference is not expected from the simulation, Figure 7-8. The decrease in the simulated values leads to much better agreement with the measurements for the September episode; the simulation is 41% higher at UC-Davis, 46% higher at Sunol and 29% higher at DRI, Table 7-2.

The simulated ratio JO_3 / JNO_2 is also much greater than the measured ratio for the July-August episode although the agreement is much better for JO_3 / JNO_2 than for JO_3 alone and the ratio is very consistent between UC-Davis and Sunol, Figure 7-10. The simulation was greater than the measurements by 71 and 81% at UC-Davis and Sunol, respectively. Table 7-2. The lower JO_3 simulated for the September episode lead to better agreement between the simulated and measured ratios of JO_3 / JNO_2, Figures7-11 and 7-12. The percent difference between the median maximum simulated values and measurements are 26, 25 and 6% at UC-Davis, Sunol and DRI, respectively, Table 7-4. The noise in the Sunol data and the daily perturbation in the DRI data are visible in the September episode plot of JO_3 / JNO_2, Figure 7-11.

For the July-August case simulations of the rate parameters for the photolysis of HCHO to produce the molecular products (HCHO + hν $\rightarrow$ H_2 + CO) were greater than the measurements but the difference was less than found for JO_3, Figures 7-13 and 7-14, Table 7-1. The simulated median maximum values of JHCHO (Molecular Reaction) are greater than the measured values by 83% at UC-Davis and 100% at Sunol. The difference between the measured JHCHO (Molecular Reaction) during the July-August and September episodes is small while the simulated values decreased by 14%. This improved agreement for the September case where simulated median maximum values were higher by 38, 44 and 47% at UC-Davis, Sunol and DRI respectively, Table 7-3.

The agreement between the simulated and measured ratio JHCHO (Molecular Reaction) / JNO_2 was better than most of the other comparisons for both episodes. Figures 7-17 and 7-18 show the measured and simulated ratio for the July-August episode. The simulated median maximum ratio is 31% higher than the measured value at UC-Davis and 37% higher at Sunol, Table 7-2. For the September episode the agreement is better, the simulated ratios are greater than the measurements by 21, 21 and 31% at UC-Davis, Sunol and DRI, respectively.

The other photolysis reaction of HCHO is its reaction to form radical products (HCHO + hν (+O_2) $\rightarrow$ 2 HO_2 and CO under atmospheric conditions). Figures 7-22 and 7-23 show that the simulated JHCHO (Radical Reaction) is much lower than the measured reaction for the July-August episode. The simulation was 109 and 130% greater than the measured median maximum values for UC-Davis and Sunol, respectively. The simulated and measured values are closer for the September episode, Figures 7-23 and 7-24. The difference between the simulated and measured values are 43, 49 and 52% at UC-Davis, Sunol and DRI, respectively, Table 7-3. For the July-August episode the simulated ratio of JHCHO (Radical Reaction) / JNO_2 are greater than the measurements by 119 and 129% at UC-Davis and Sunol, respectively, while for the September episode the simulated ratio of JHCHO (Radical Reaction) / JNO_2 are greater than the measurements by 52, 52 and 59% at UC-Davis, Sunol and DRI.

Finally shadowband radiometer data was available from the U.S. Department of Agriculture UV-B Monitoring and Research Program located at UC-Davis. Shadowband radiometers are flat plate radiometers that are equipped with rotating metal bands that

periodically block the direct solar beam from the detector. This allows the total horizontal, diffuse and direct normal components of the solar radiation to be determined.

The shadowband radiometer data at a wavelength of 300 nm from UC-Davis is plotted in Figures 7-29 and 7-30 for both episodes. The shadowband data is consistent with the photolysis rate constants for the July-August episode. August 1 appears to have been affected by clouds. The September episode shows considerable day-to-day variation in the peak shadowband flux and this variation is seen in the ozone photolysis rate parameter but the relative variation appears to be less. It is possible that by combining the data from this research with the USDA data from UC-Davis that better photolysis rate parameters could be calculated, but that is beyond the current scope of this project.

Figure 7-1. Photolysis rate parameters of NO_2 measured at UC-Davis and Sunol for episode July 30 to August 2, 2000.

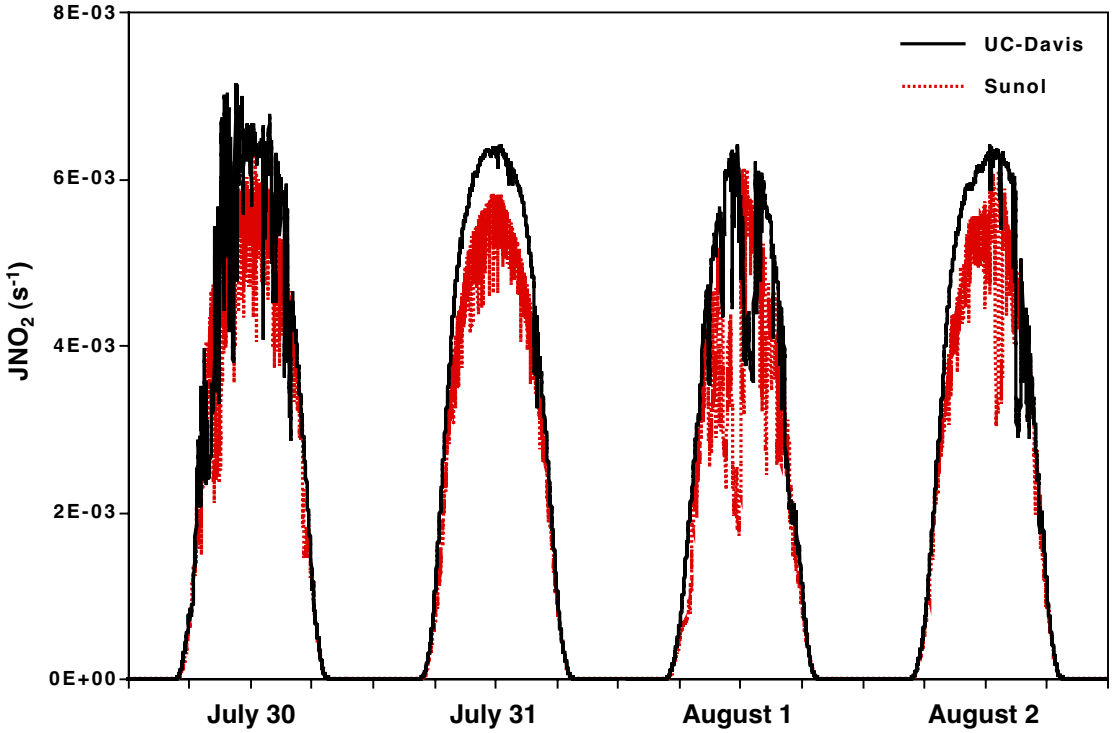

Figure 7-2. Simulated photolysis rate parameters of NO_2 at UC-Davis and Sunol for episode July 30 to August 2, 2000.

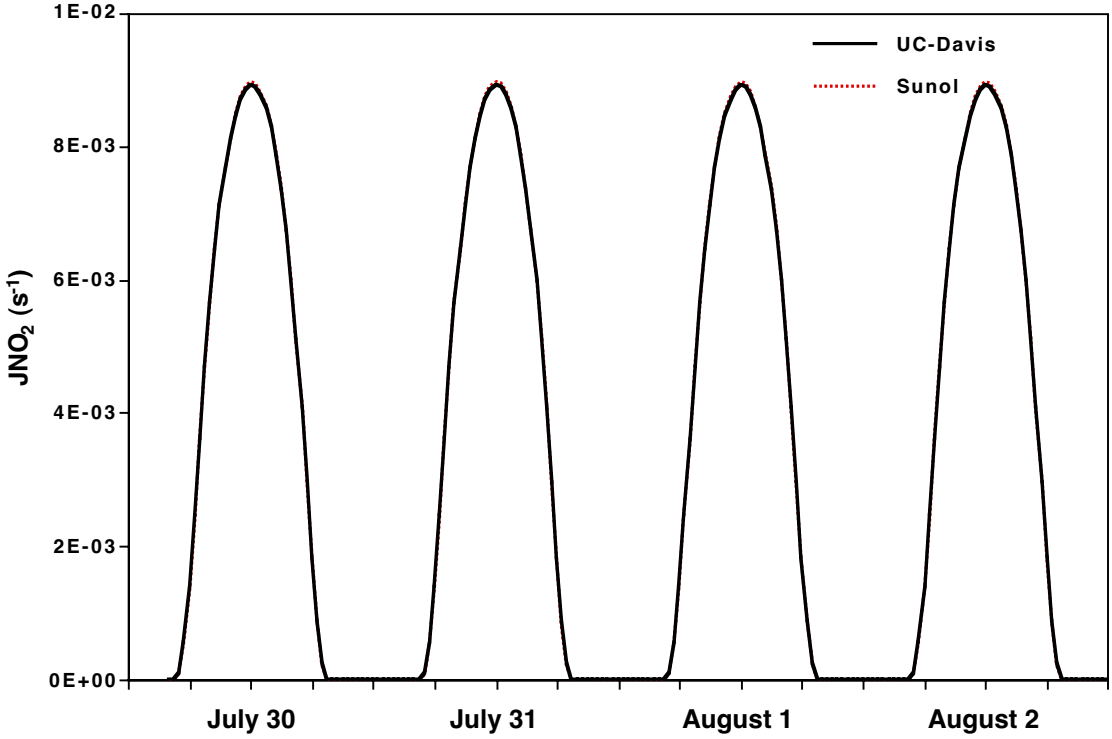

Figure 7-3. Photolysis rate parameters of NO_2 measured at UC-Davis, Sunol and DRI for episode September 17 to 21, 2000.

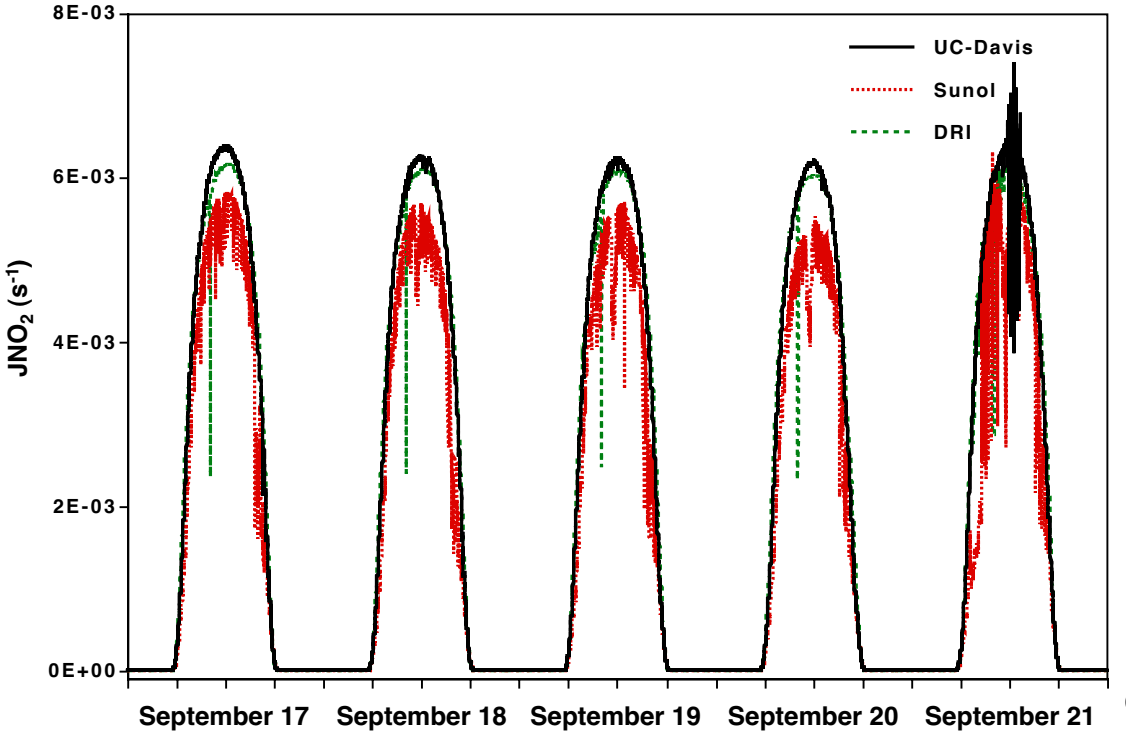

Figure 7-4. Simulated photolysis rate parameters of NO_2 at UC-Davis, Sunol and DRI for episode September 17 to 21, 2000.

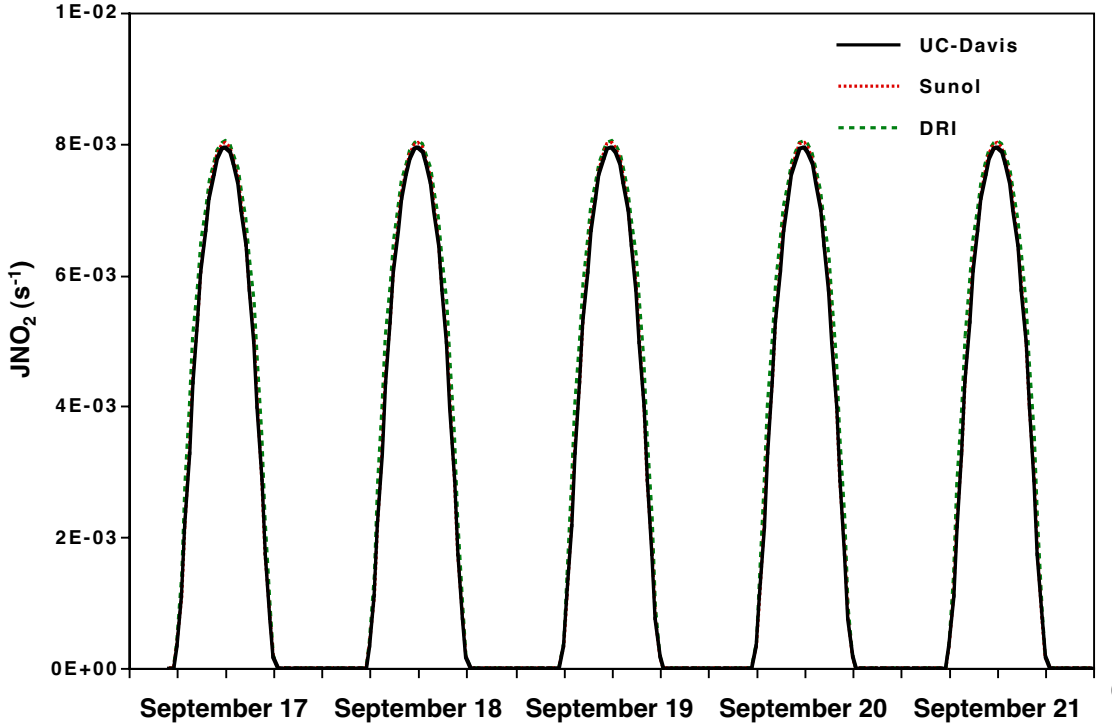

Figure 7-5. Photolysis rate parameters of O_3 measured at UC-Davis and Sunol for episode July 30 to August 2, 2000.

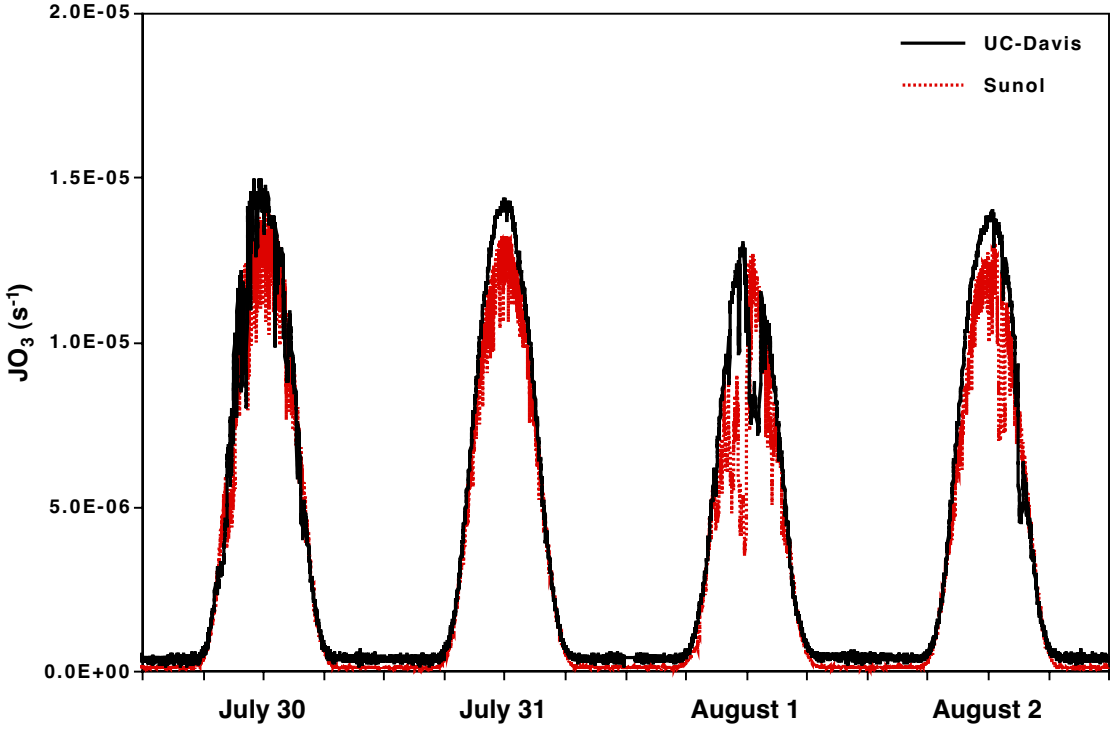

Figure 7-6. Simulated rate parameters of O_3 at UC-Davis and Sunol for episode July 30 to August 2, 2000.

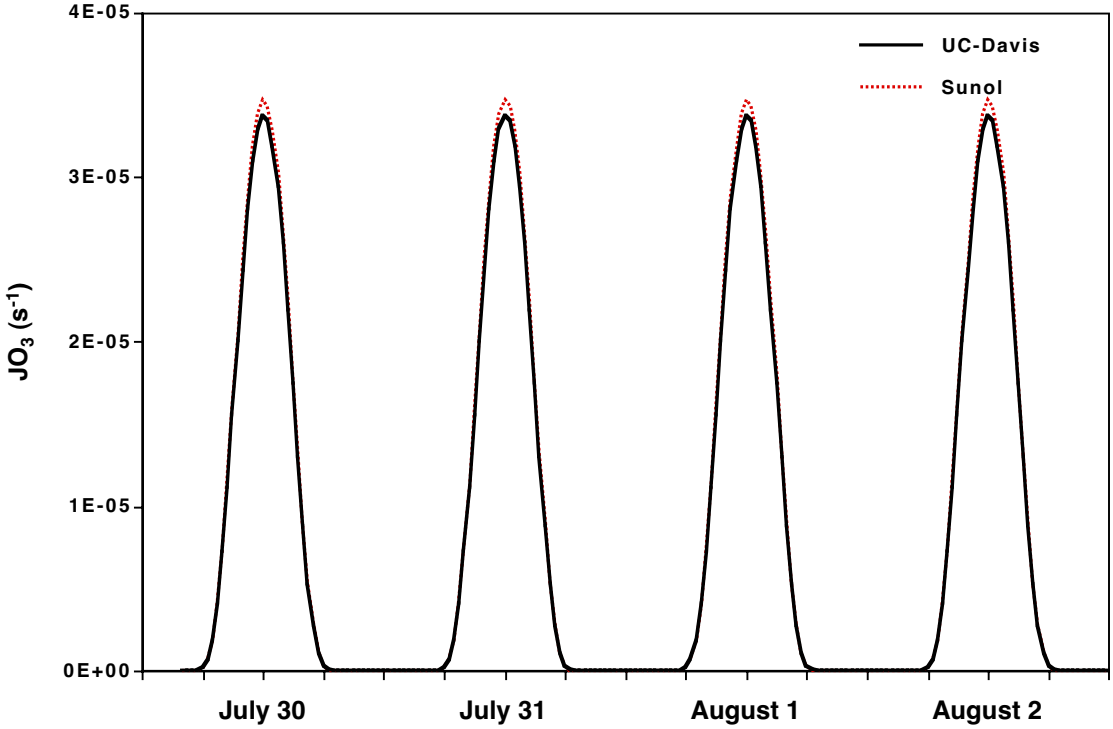

Figure 7-7. Photolysis rate parameters of O_3 measured at UC-Davis, Sunol and DRI for episode September 17 to 21, 2000.

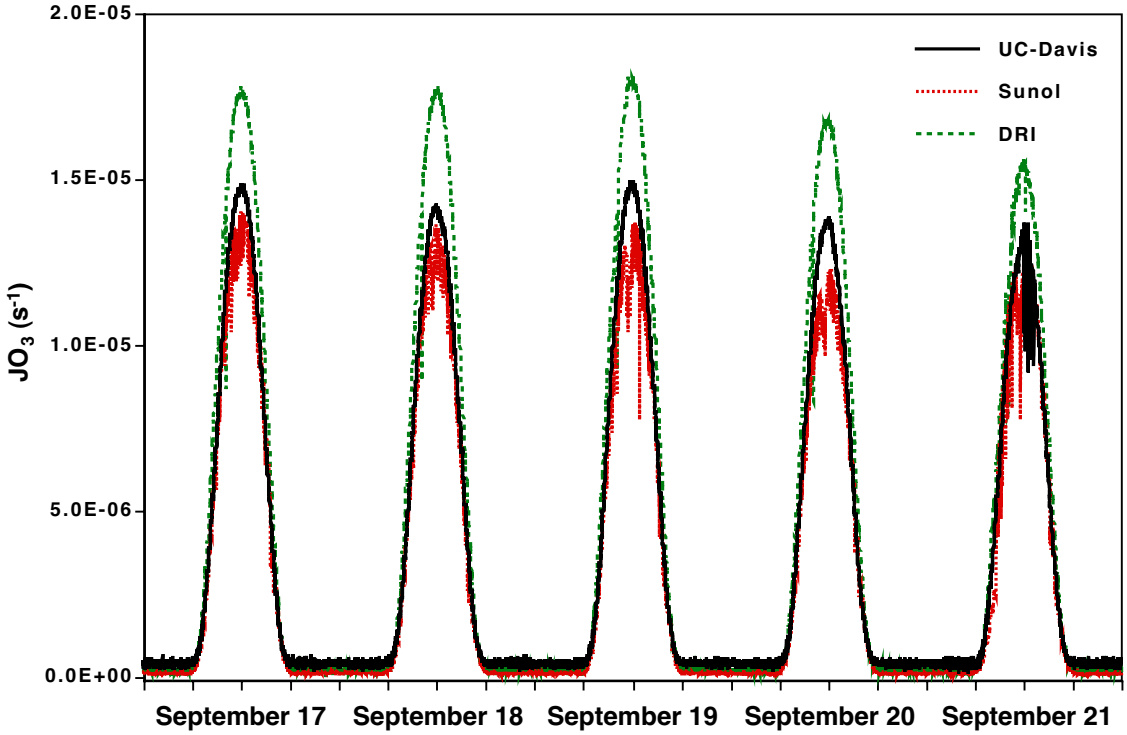

Figure 7-8. Simulated photolysis rate parameters of O_3 at UC-Davis, Sunol and DRI for episode September 17 to 21, 2000.

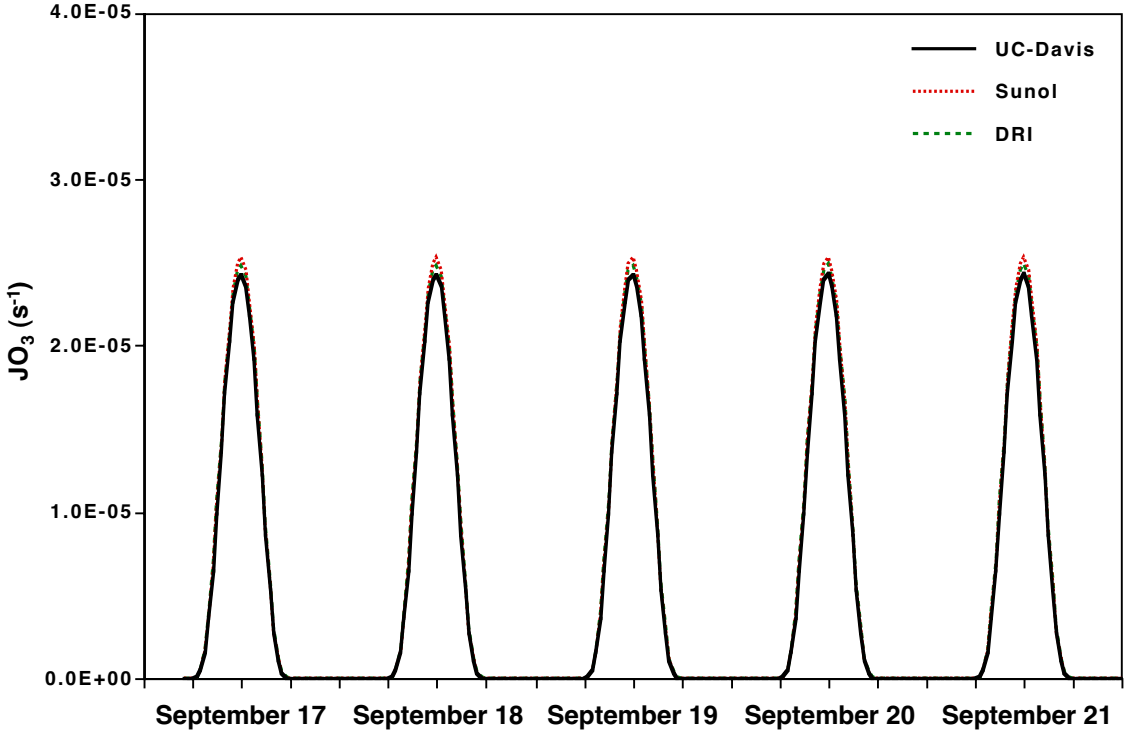

Figure 7-9. Ratio of photolysis rate parameters of O_3 to photolysis rate parameters of NO_2 measured at UC-Davis and Sunol for episode July 30 to August 2.

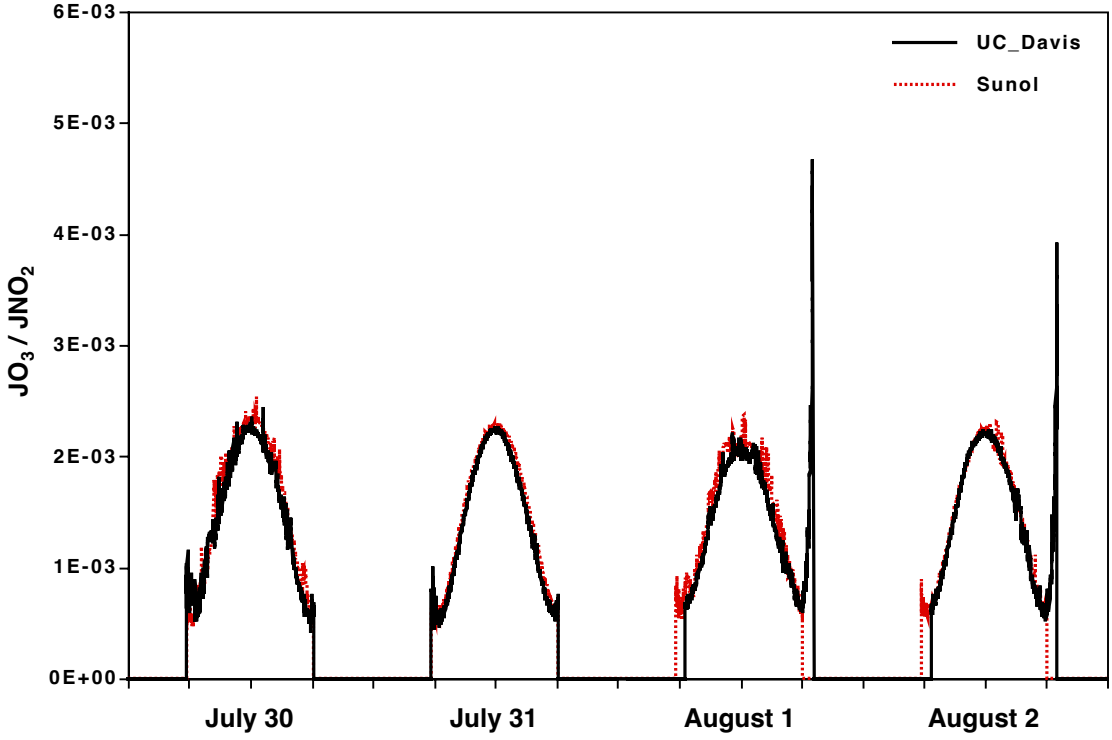

Figure 7-10. Simulated ratio of photolysis rate parameters of O_3 to photolysis rate parameters of NO_2 at UC-Davis and Sunol for episode July 30 to August 2.

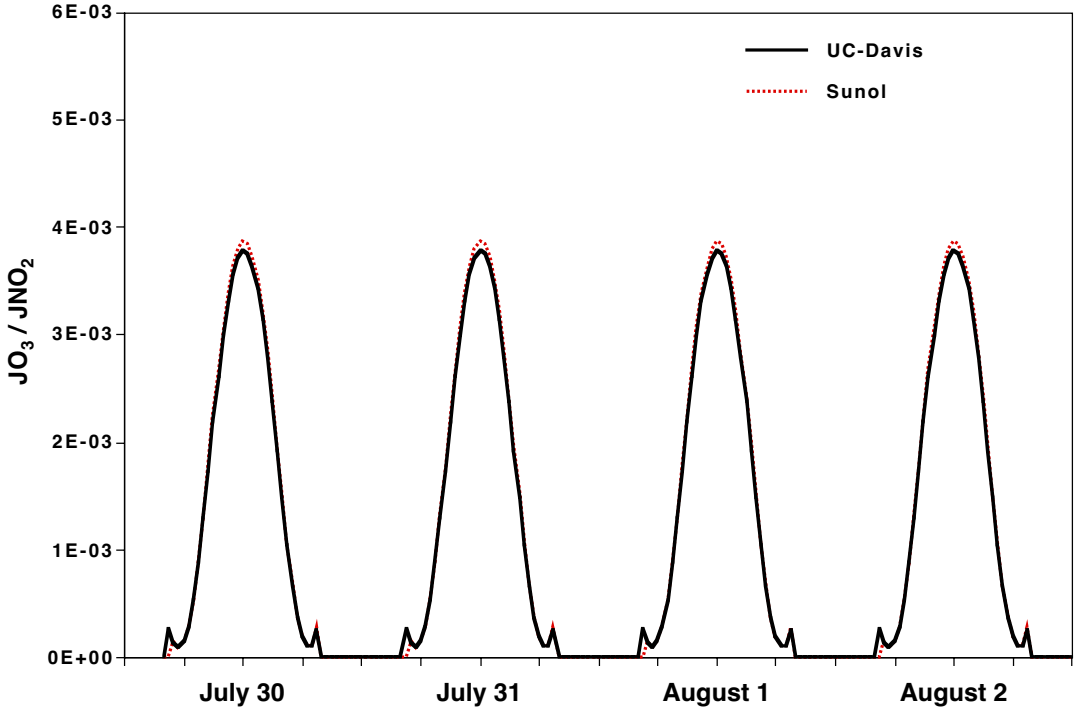

Figure 7-11. Ratio of photolysis rate parameters of O_3 to photolysis rate parameters of NO_2 measured at UC-Davis, Sunol and DRI for episode September 17 to 21.

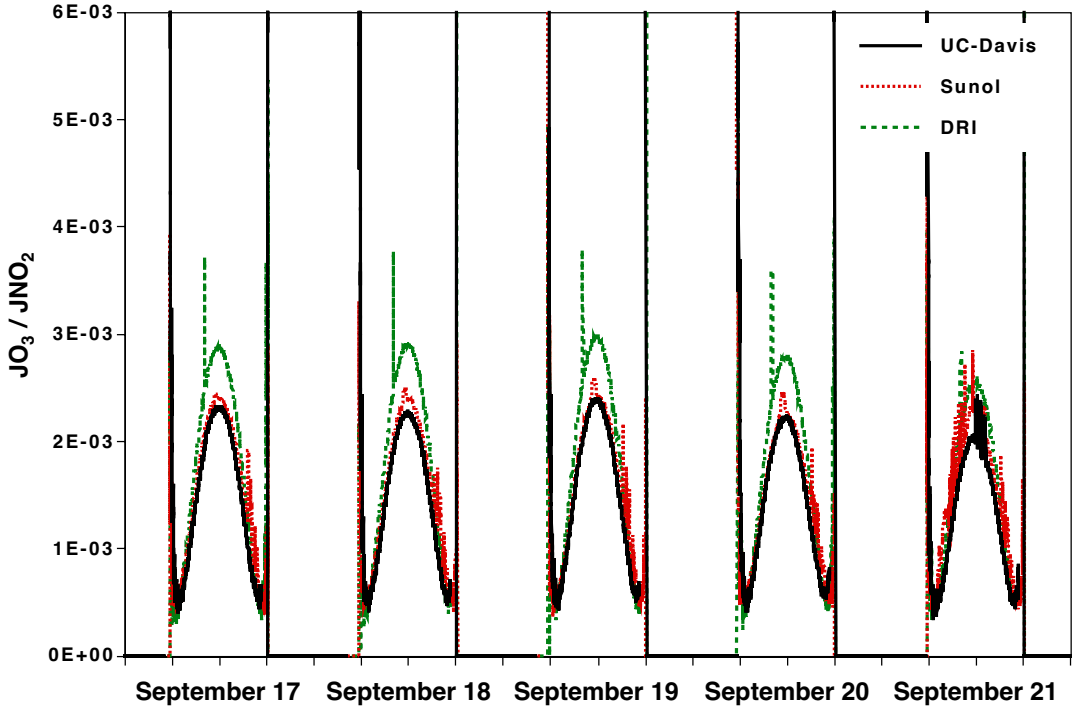

Figure 7-12. Simulated ratio of photolysis rate parameters of O_3 to photolysis rate parameters of NO_2 at UC-Davis, Sunol and DRI for episode September 17 to 21.

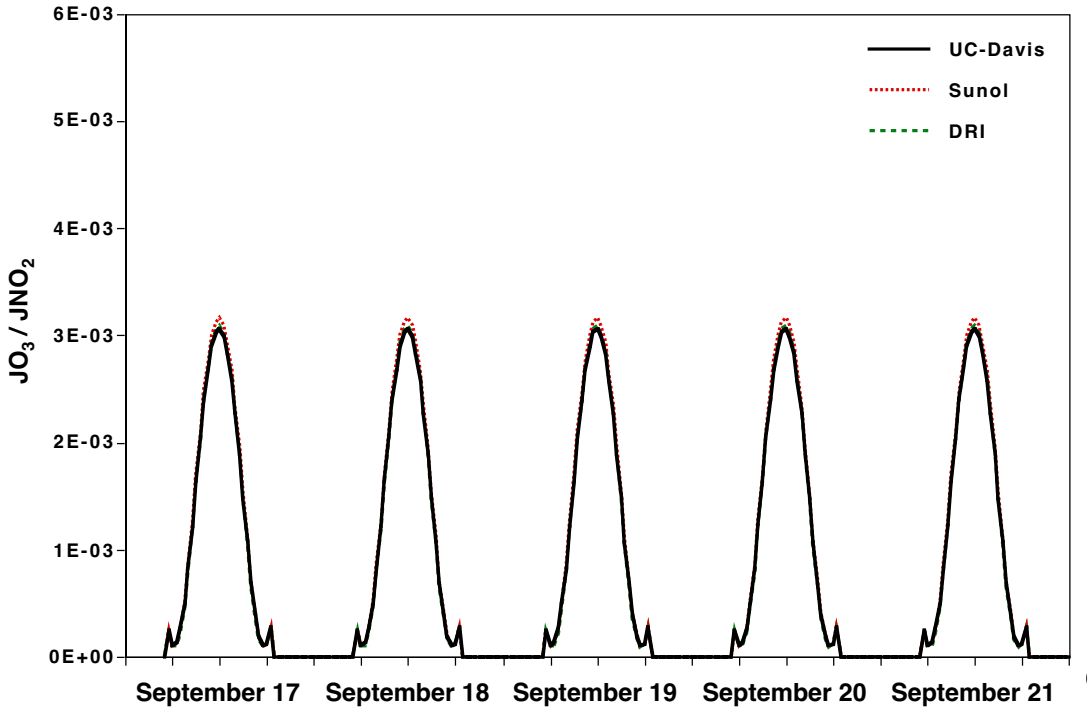

Figure 7-13. Photolysis rate parameters of HCHO reaction to form molecular products measured at UC-Davis and Sunol for episode July 30 to August 2, 2000.

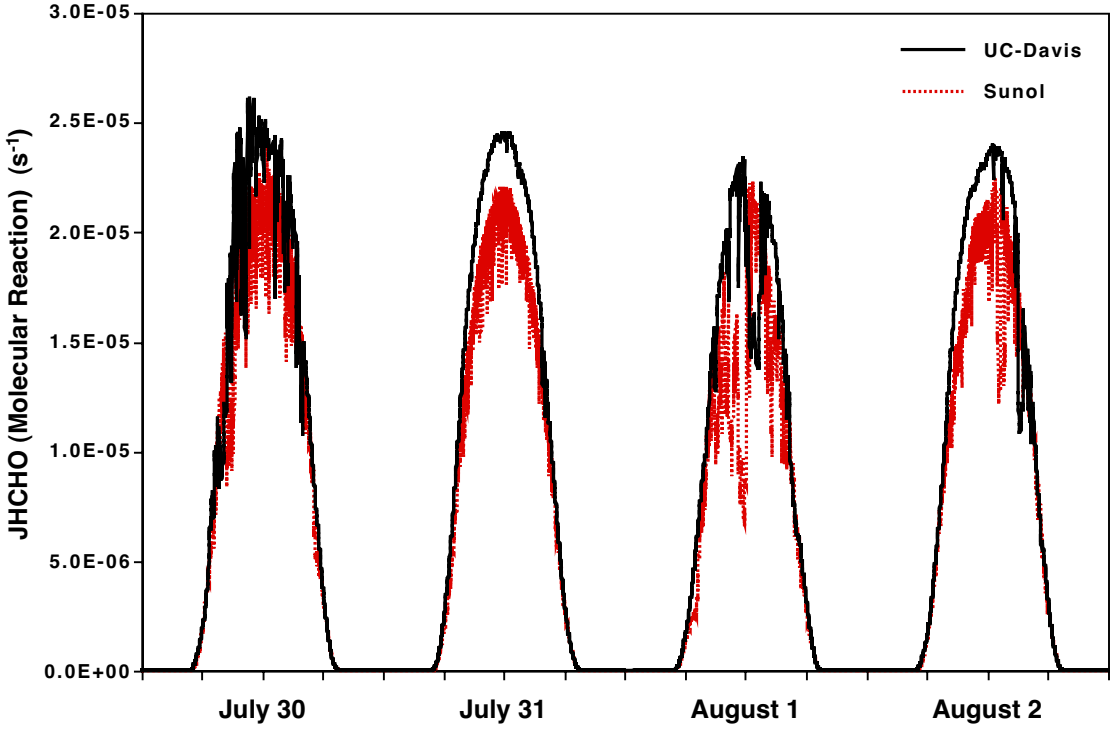

Figure 7-14. Simulated photolysis rate parameters of HCHO reaction to form molecular products at UC-Davis and Sunol for episode July 30 to August 2, 2000.

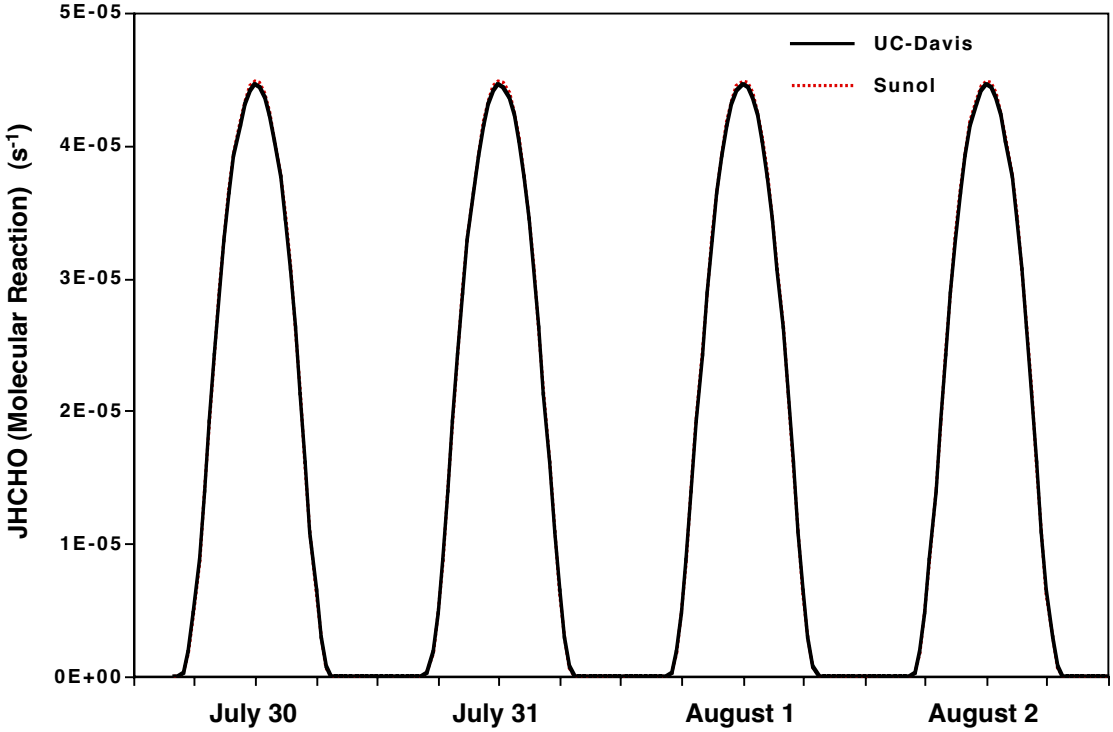

Figure 7-15. Photolysis rate parameters of HCHO reaction to form molecular products measured at UC-Davis, Sunol and DRI for episode September 17 to 21, 2000.

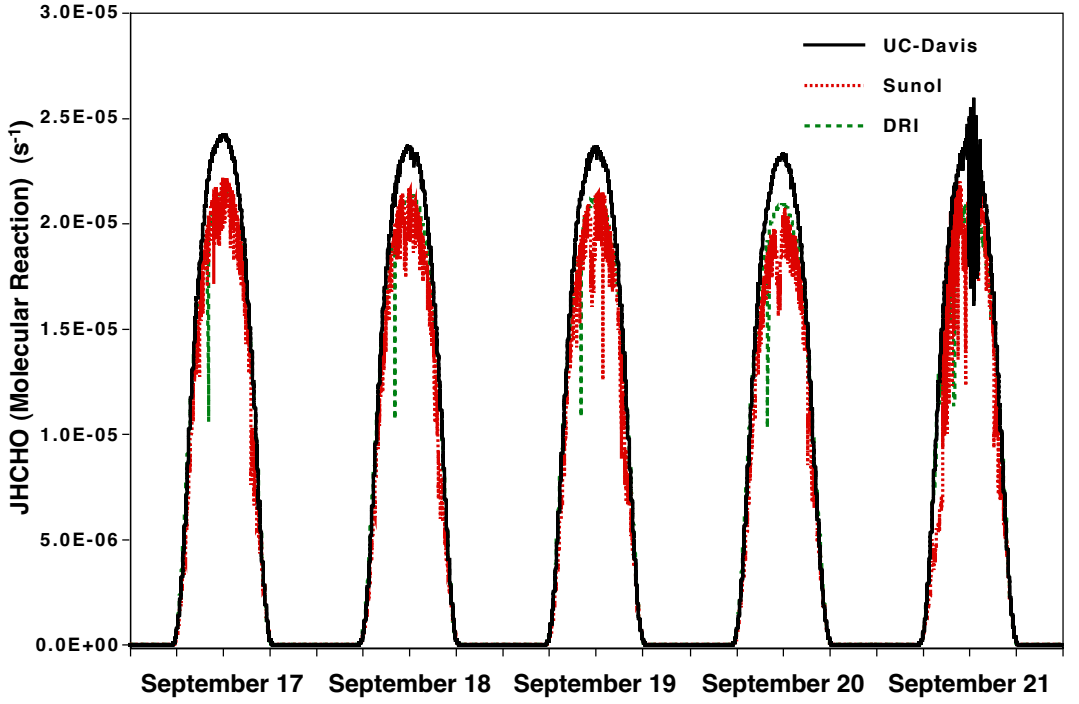

Figure 7-16. Simulated photolysis rate parameters of HCHO reaction to form molecular products at UC-Davis, Sunol and DRI for episode September 17 to 21, 2000.

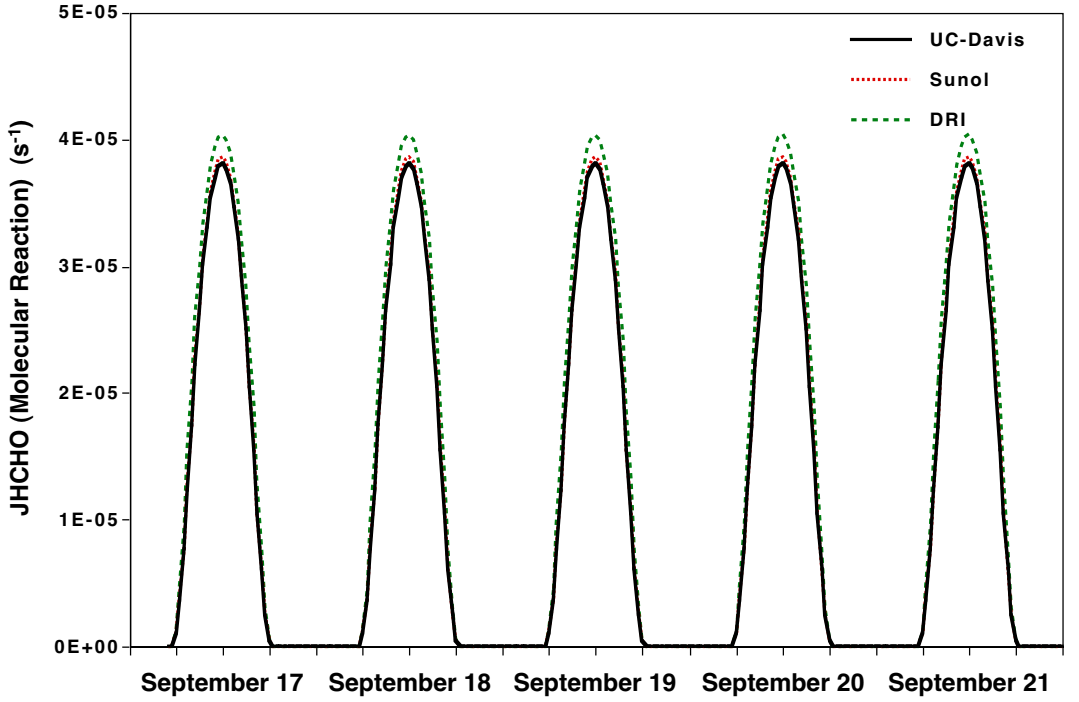

Figure 7-17. Ratio of photolysis rate parameters of HCHO reaction to form molecular products to photolysis rate parameters of NO_2 measured at UC-Davis and Sunol for episode July 30 to August 2, 2000.

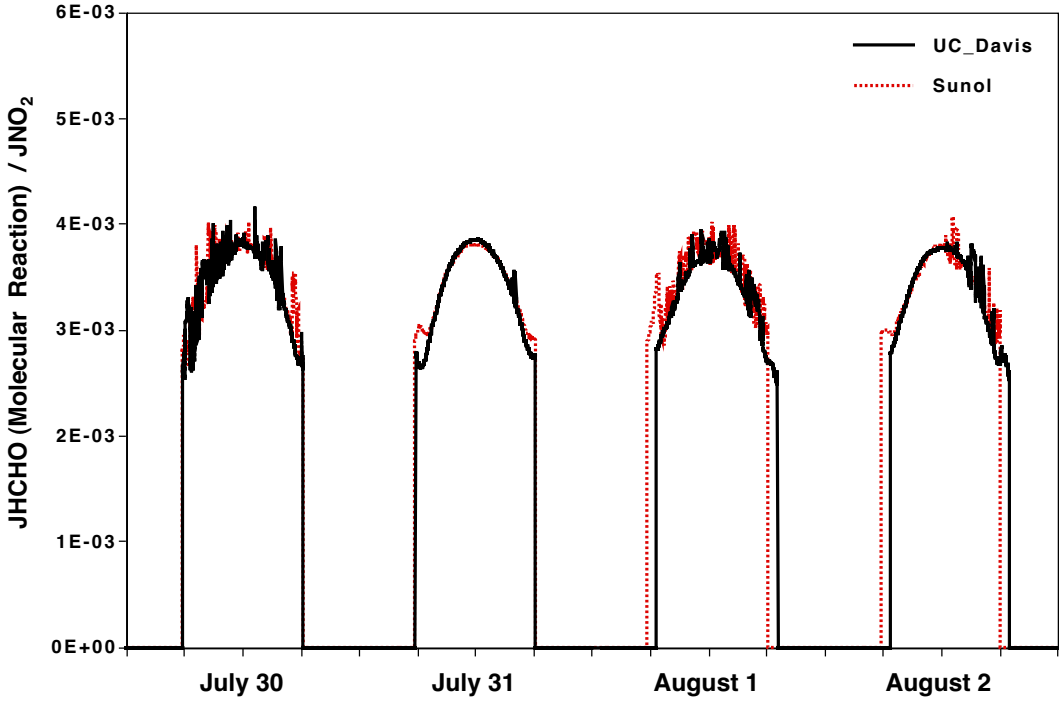

Figure 7-18. Simulated ratio of photolysis rate parameters of HCHO reaction to form molecular products to photolysis rate parameters of NO_2 at UC-Davis and Sunol for episode July 30 to August 2, 2000.

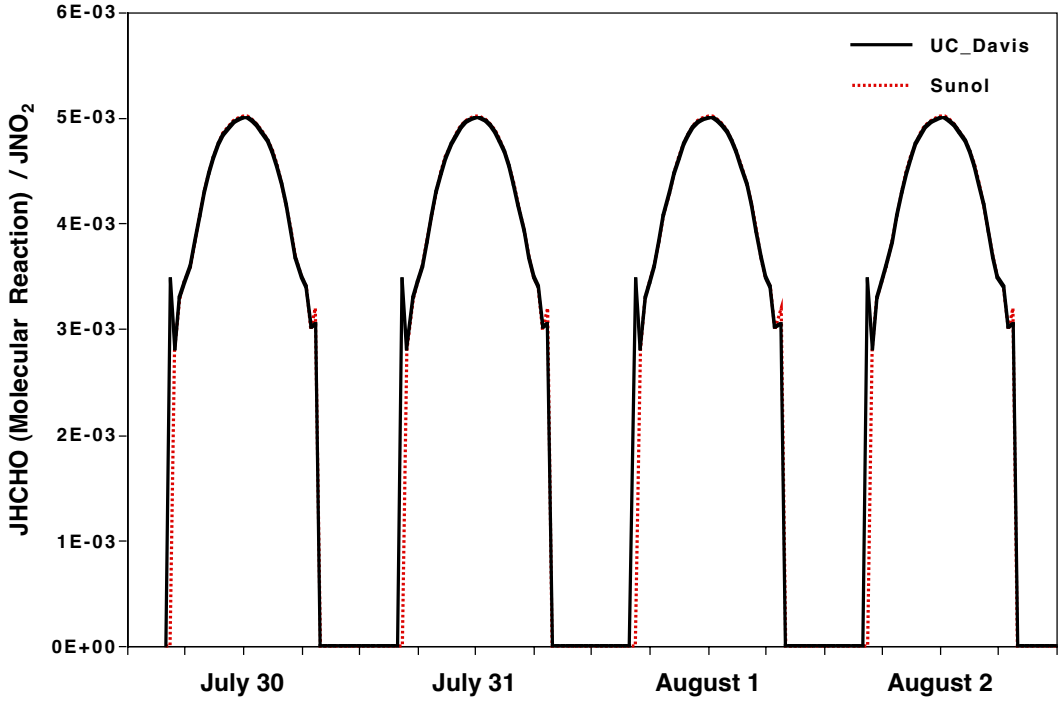

Figure 7-19. Ratio of photolysis rate parameters of HCHO reaction to form molecular products to photolysis rate parameters of NO_2 measured at UC-Davis, Sunol and DRI for episode September 17 to 21, 2000.

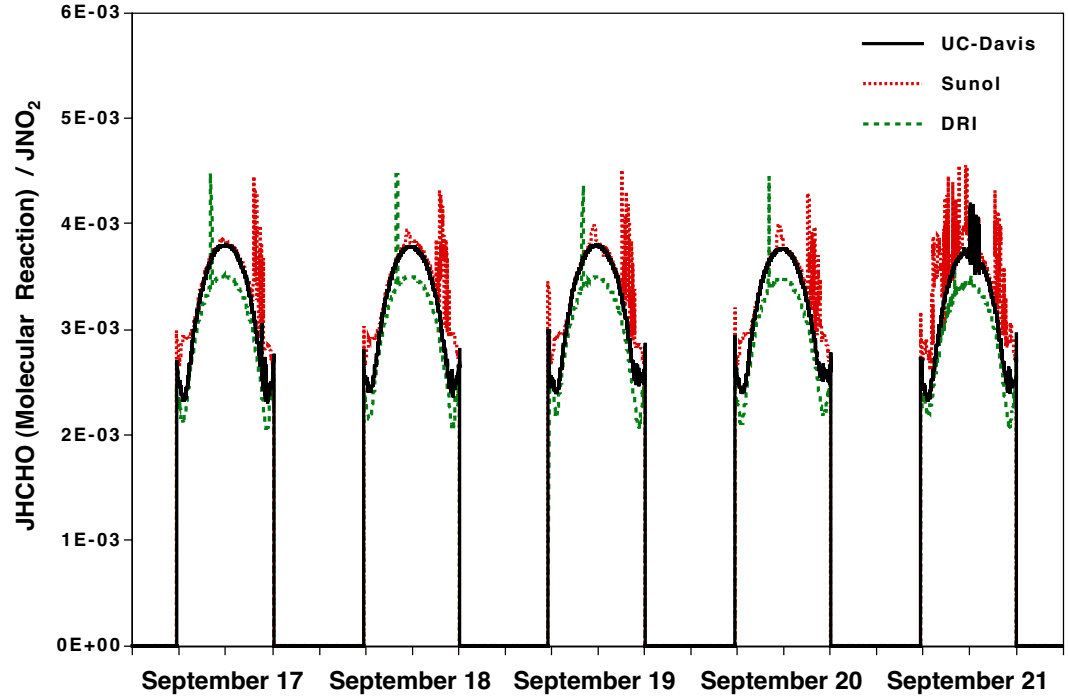

Figure 7-20. Simulated ratio of photolysis rate parameters of HCHO reaction to form molecular products to photolysis rate parameters of NO_2 at UC-Davis and Sunol for UC-Davis, Sunol and DRI for episode September 17 to 21, 2000.

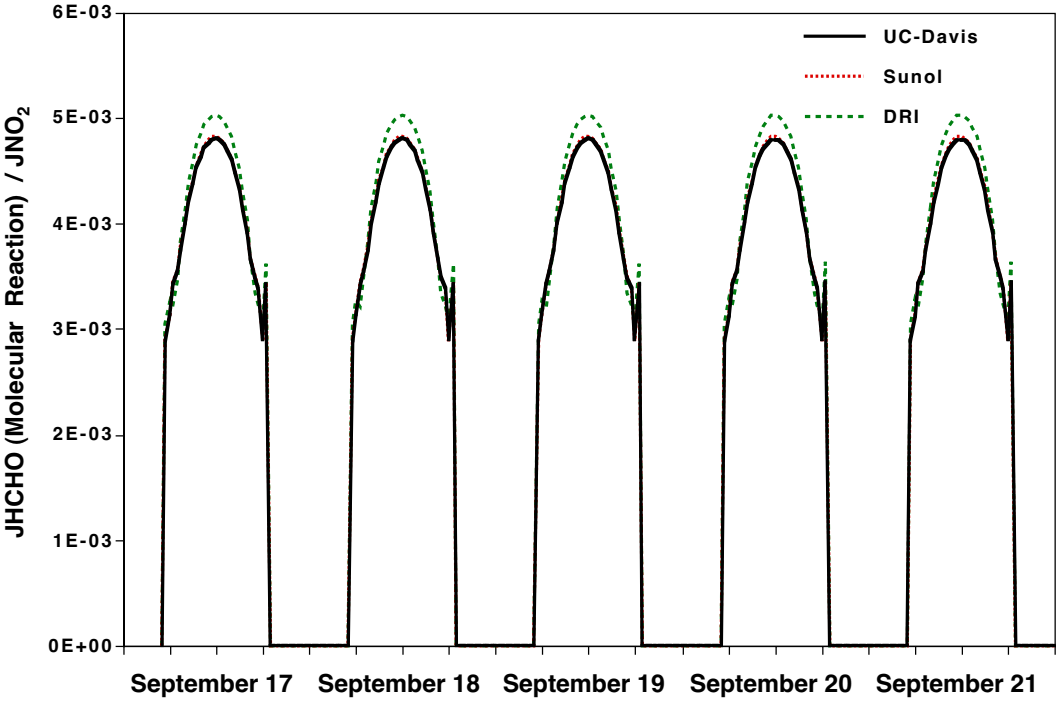

Figure 7-21. Photolysis rate parameters of HCHO reaction to form radical products measured at UC-Davis and Sunol for episode July 30 to August 2, 2000.

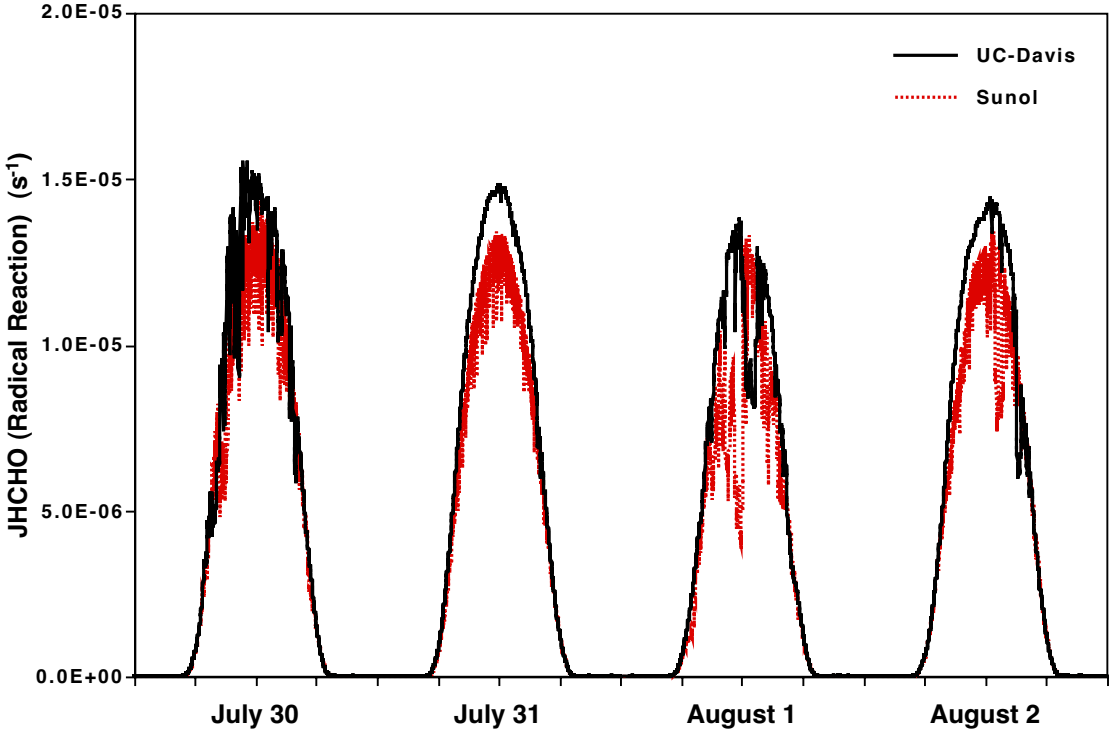

Figure 7-22. Simulated photolysis rate parameters of HCHO reaction to form radical products at UC-Davis and Sunol for episode July 30 to August 2, 2000.

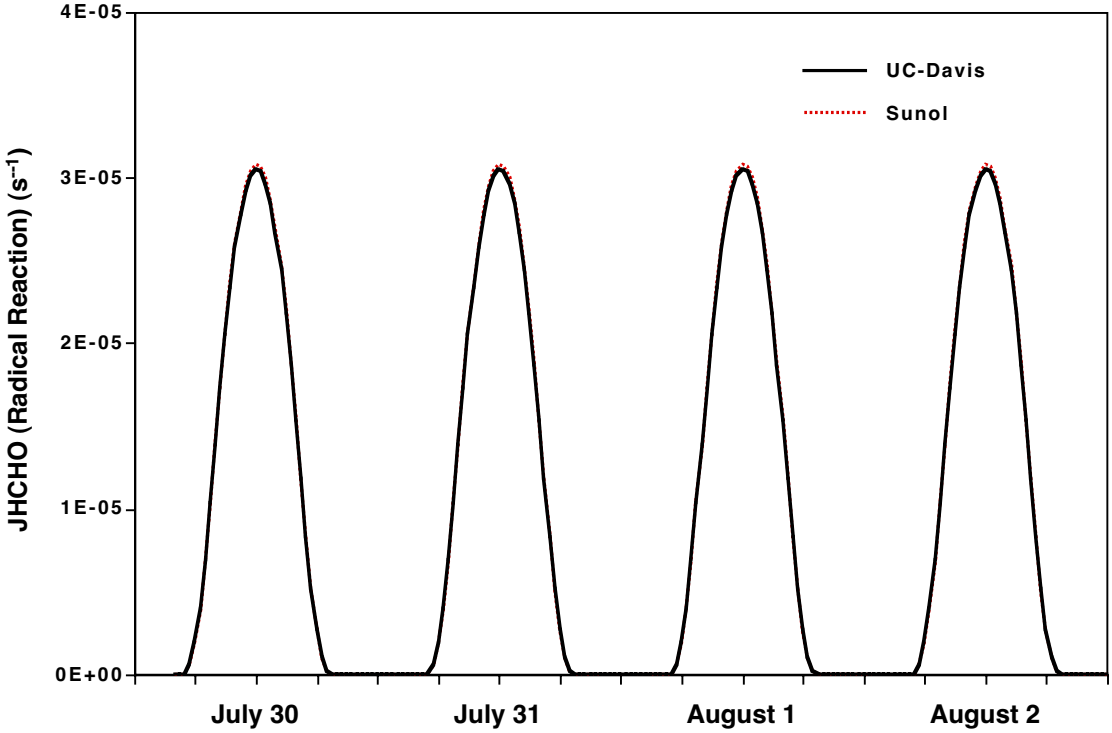

Figure 7-23. Photolysis rate parameters of HCHO reaction to form radical products measured at UC-Davis, Sunol and DRI for episode September 17 to 21, 2000.

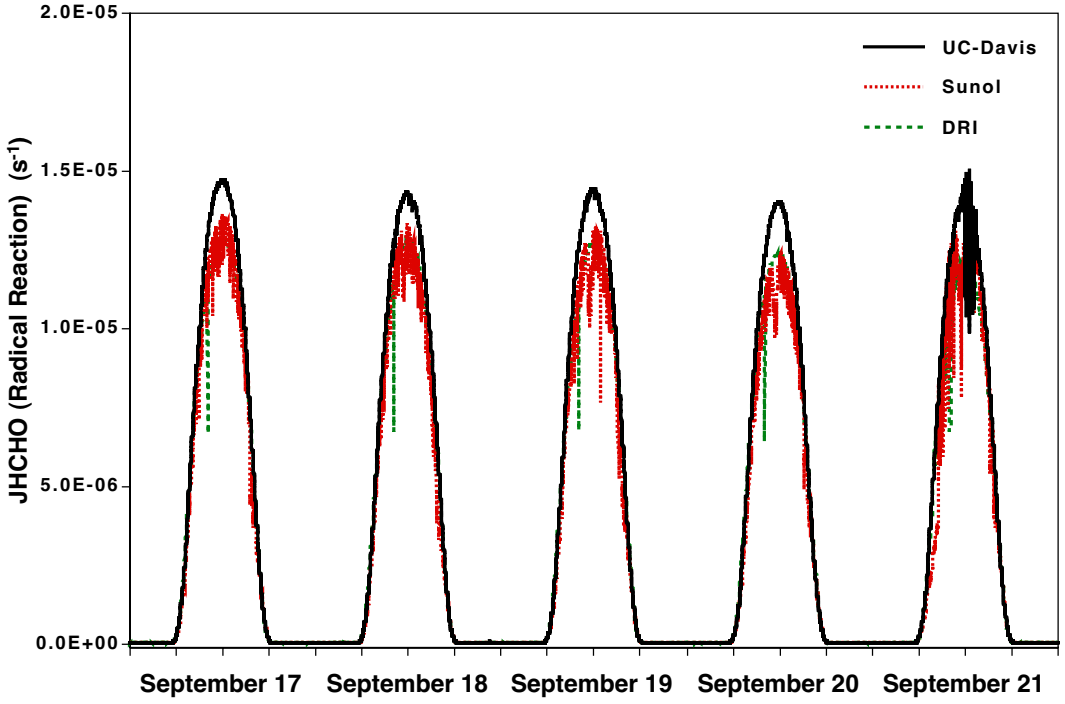

Figure 7-24. Simulated photolysis rate parameters of HCHO reaction to form radical products at UC-Davis, Sunol and DRI for episode September 17 to 21, 2000.

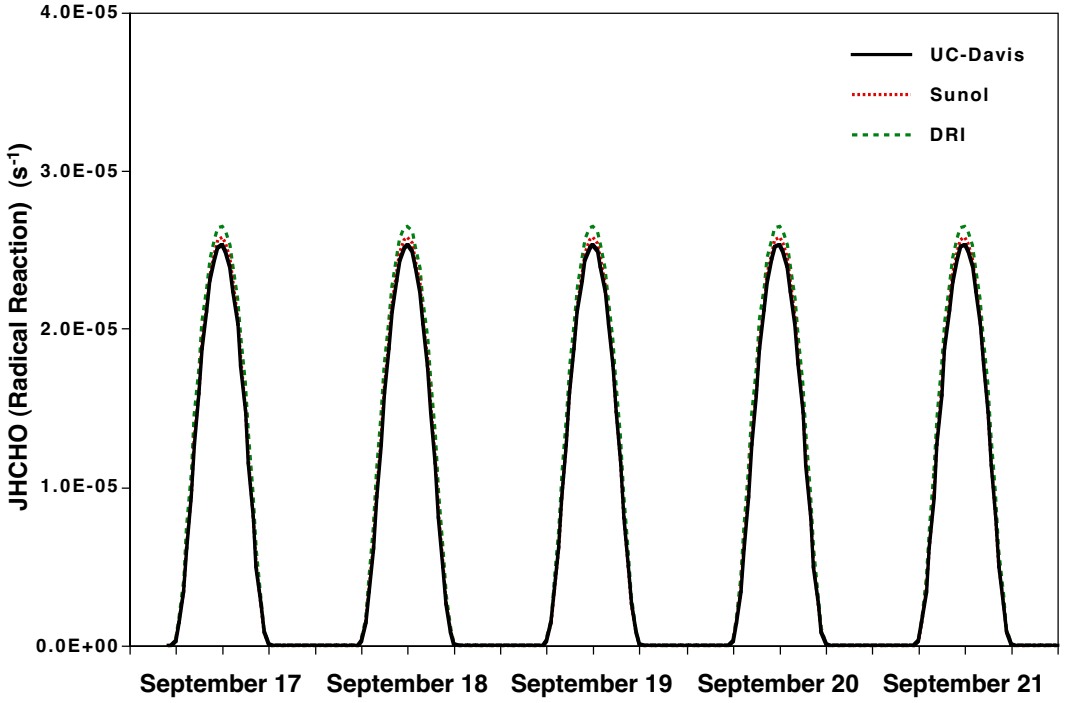

Figure 7-25. Ratio of photolysis rate parameters of HCHO reaction to form radical products to photolysis rate parameters of NO_2 measured at UC-Davis and Sunol for episode July 30 to August 2, 2000.

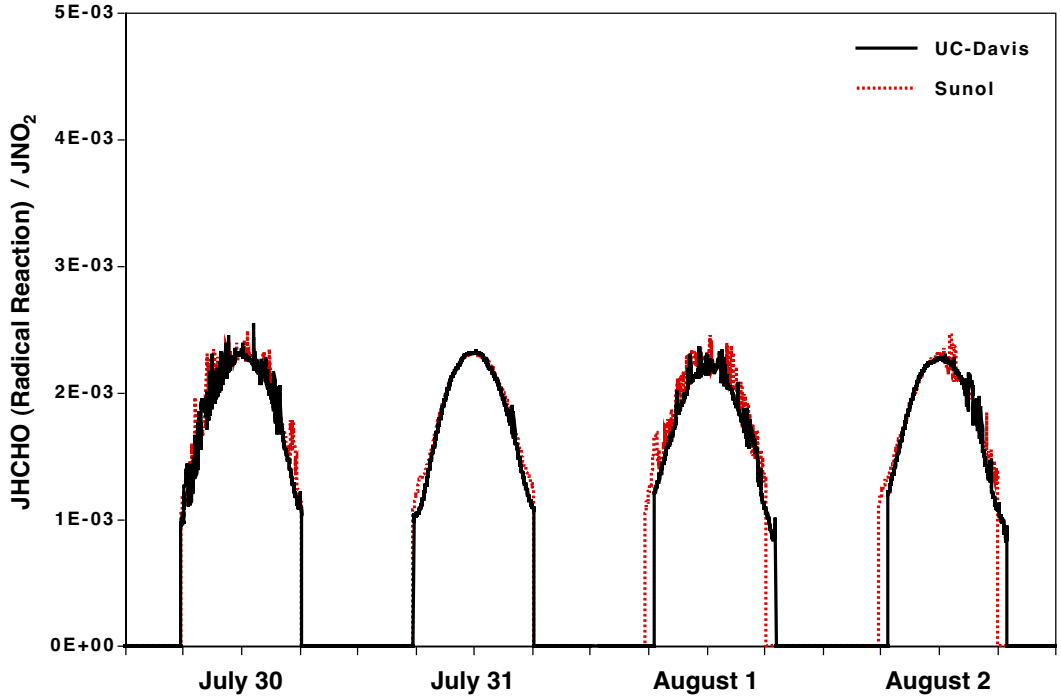

Figure 7-26. Simulated ratio of photolysis rate parameters of HCHO reaction to form radical products to photolysis rate parameters of NO_2 at UC-Davis and Sunol for episode July 30 to August 2, 2000.

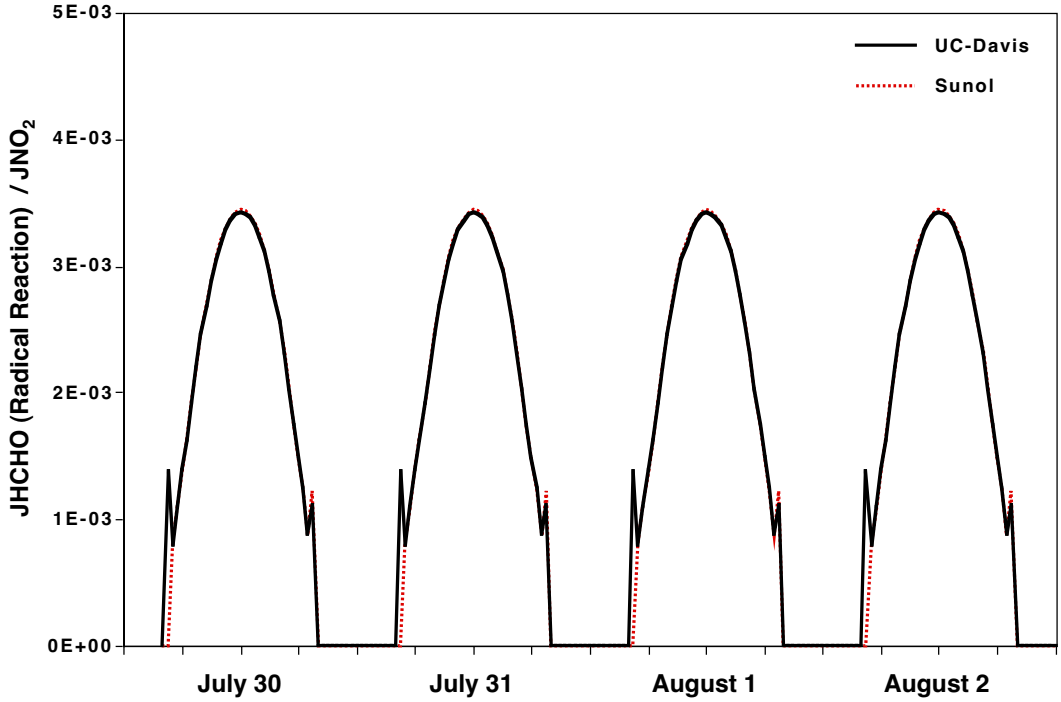

Figure 7-27. Ratio of photolysis rate parameters of HCHO reaction to form radical products to photolysis rate parameters of NO_2 measured at UC-Davis, Sunol and DRI for episode September 17 to 21, 2000.

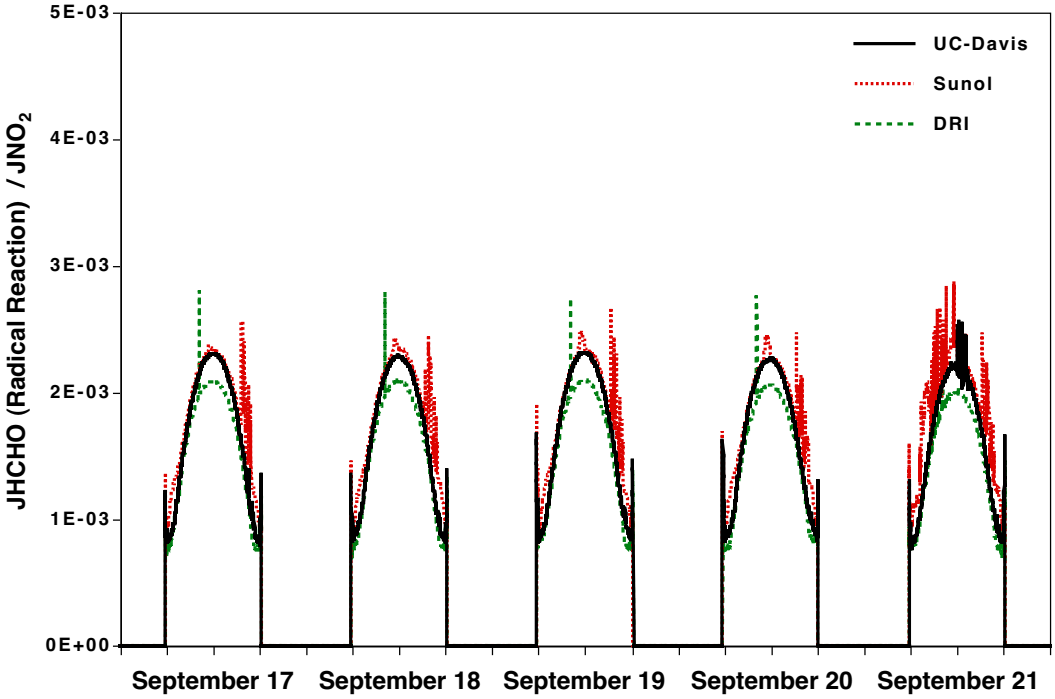

Figure 7-28. Simulated ratio of photolysis rate parameters of HCHO reaction to form radical products to photolysis rate parameters of NO_2 at UC-Davis and Sunol for UC-Davis, Sunol and DRI for episode September 17 to 21, 2000.

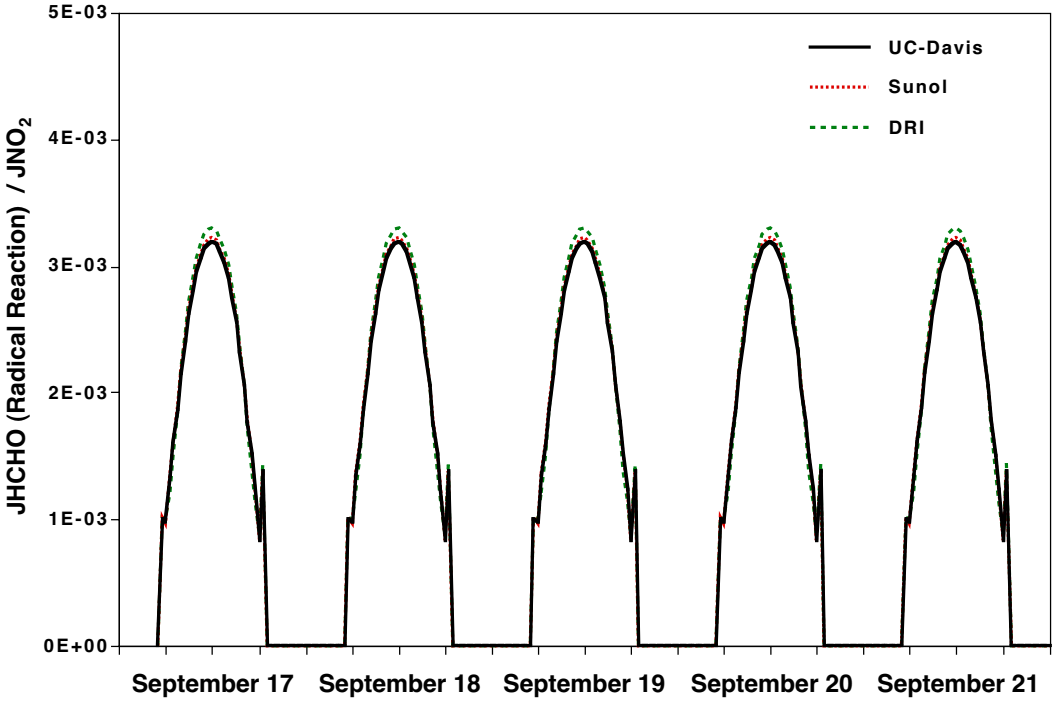

Table 7-1. Median maximum photolysis rate parameters measured and simulated for the episode July 30 to August 20 and their percent differences (using the measurements as reference values).

	JNO_2 (s-1)	JO_3 (s-1)	JHCHO (Molecular Reaction) (s-1)	JHCHO (Radical Reaction) (s-1)
Simulation				
UC-Davis	8.917E-03	3.372E-05	4.457E-05	3.051E-05
Sunol	8.955E-03	3.467E-05	4.488E-05	3.083E-05
Measurements				
UC-Davis	6.39E-03	1.41E-05	2.43E-05	1.46E-05
Sunol	6.12E-03	1.31E-05	2.24E-05	1.34E-05
Percent Difference				
UC-Davis	40%	139%	83%	109%
Sunol	46%	165%	100%	130%

Table 7-2. Ratio of median maximum photolysis rate parameters to the photolysis rate parameter of NO_2 measured and simulated for the episode July 30 to August 20 and their percent differences (using the measurements as reference values).

	JO_3 / JNO_2	JHCHO (Molecular Reaction) / JNO_2	JHCHO (Radical Reaction) / JNO_2
Simulation			
UC-Davis	3.782E-03	4.998E-03	3.422E-03
Sunol	3.871E-03	5.012E-03	3.443E-03
Measurements			
UC-Davis	2.21E-03	3.80E-03	2.28E-03
Sunol	2.14E-03	3.66E-03	2.19E-03
Percent Difference			
UC-Davis	71%	31%	119%
Sunol	81%	37%	129%

Figure 7-29. Shadowband radiometer data at a wavelength of 300 nm from UC-Davis site for episode July 30 to August 2. The data is provided by the U.S. Department of Agriculture UV-B Monitoring and Research Program, Natural Resource Ecology Laboratory, Colorado State University.

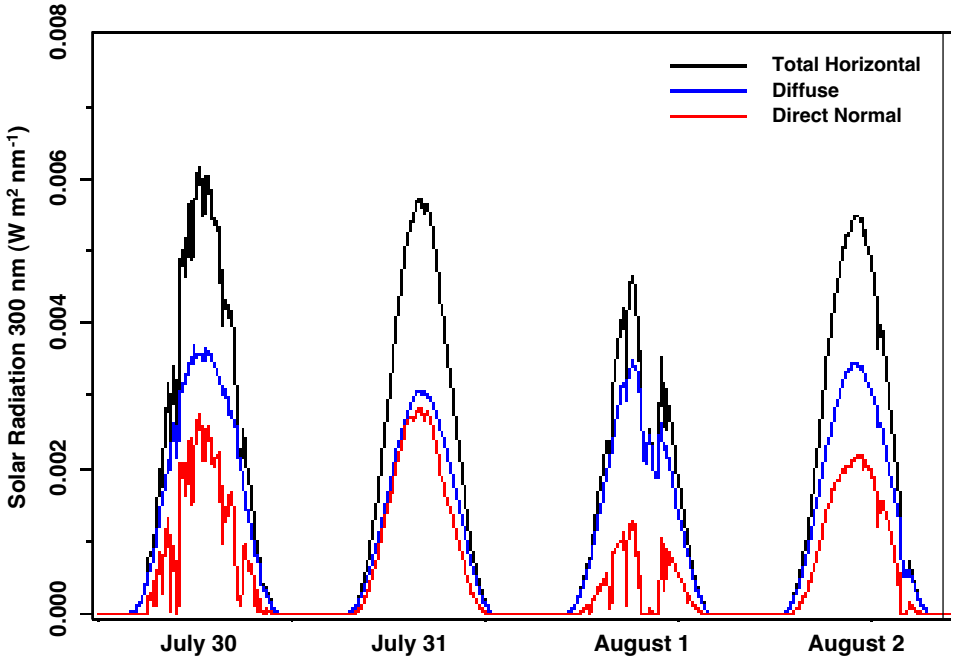

Figure 7-29. Shadowband radiometer data at a wavelength of 300 nm from UC-Davis site for the episode September 17 to 21. The data is provided by the U.S. Department of Agriculture UV-B Monitoring and Research Program, Natural Resource Ecology Laboratory, Colorado State University.

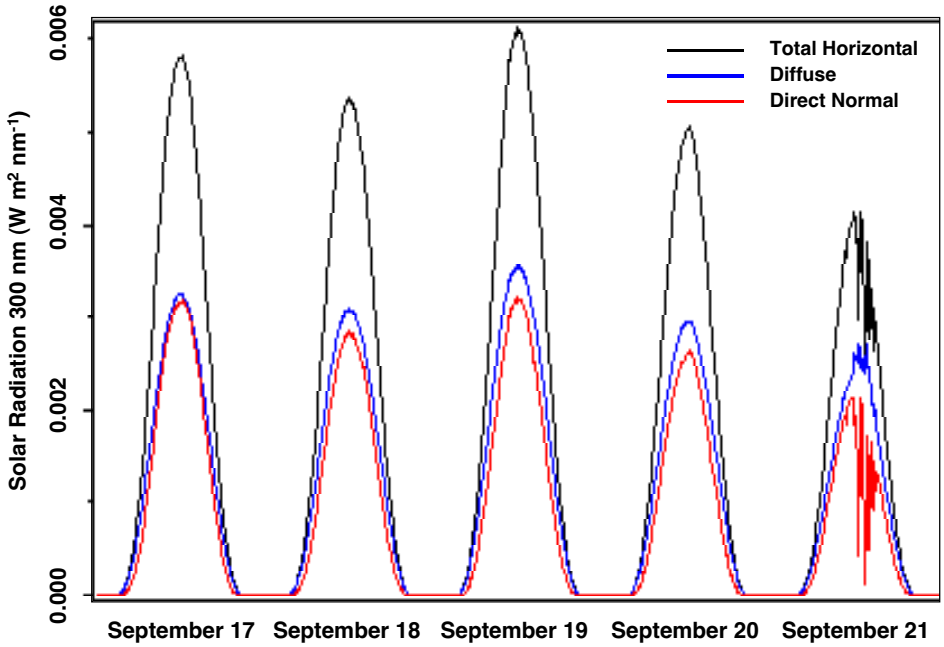

Table 7-3. Median maximum photolysis rate parameters measured and simulated for the episode September 17-21 and their percent differences (using the measurements as reference values).

	JNO_2 (s-1)	JO_3 (s-1)	JHCHO (Molecular Reaction) (s-1)	JHCHO (Radical Reaction) (s-1)
Simulation				
UC-Davis	7.938E-03	2.429E-05	3.812E-05	2.534E-05
Sunol	8.011E-03	2.532E-05	3.865E-05	2.581E-05
DRI	8.033E-03	2.485E-05	4.036E-05	2.652E-05
Measurements				
UC-Davis	6.26E-03	1.42E-05	2.37E-05	1.44E-05
Sunol	5.69E-03	1.36E-05	2.17E-05	1.33E-05
DRI	6.11E-03	1.78E-05	2.13E-05	1.27E-05
Percent Difference				
UC-Davis	21%	41%	38%	43%
Sunol	29%	46%	44%	49%
DRI	24%	29%	47%	52%

Table 7-4. Ratio of median maximum photolysis rate parameters to the photolysis rate parameter of NO_2 measured and simulated for the episode September 17-21 and their percent differences (using the measurements as reference values).

	JO_3 / JNO_2	JHCHO (Molecular Reaction) / JNO_2	JHCHO (Radical Reaction) / JNO_2
Simulation			
UC-Davis	3.060E-03	4.802E-03	4.802E-03
Sunol	3.161E-03	4.825E-03	4.825E-03
DRI	3.093E-03	5.024E-03	5.024E-03
Measurements			
UC-Davis	2.27E-03	3.78E-03	2.31E-03
Sunol	2.38E-03	3.81E-03	2.33E-03
DRI	2.91E-03	3.48E-03	2.08E-03
Percent Difference			
UC-Davis	26%	21%	52%
Sunol	25%	21%	52%
DRI	6%	31%	59%

8. Conclusions

Spectral-radiometers were used to measure actinic flux for CCOS at sites located at UC-Davis, Sunol and DRI. The solar radiation was collected with integrating hemispheric collectors and analyzed by a diode array spectrometer. The data was converted to spherically integrated actinic flux by multiplying the downward-welling radiation by an albedo correction function. The actinic flux data from Sunol showed unnatural curvature therefore the calibration of the Sunol instrument was normalized to the calibration of the UC-Davis instrument. The Sunol instrument showed appreciable noise so further use of its data may benefit from smoothing.

The actinic flux data along with the appropriate absorption cross sections and quantum yields was used to calculate the photolysis rate parameters of NO_2, O_3 and both the molecular and radical producing reactions of HCHO. The rate parameters were compared with simulated values and in every case the simulation was greater than the values derived from the measurements. The differences were greater for the July-August episode than for the September episode. The simulated and measured photolysis rate parameters of NO_2 were in closer agreement than the photolysis rate parameters of O_3 and HCHO. The lower measured photolysis rate parameters of O_3 and HCHO could be due in part to a lack of sensitivity and poor signal-to-noise ratios at the lower wavelengths of the diode array but this seems less likely for NO_2. The albedo correction function may be too low but it ranges from about 1.08 to over 1.2. An increase in the photolysis rate parameters by due to errors in the albedo correction function is possible but the simulated values would remain greater than the measured values.

It seems probable based on these measurements that the actual photolysis rate parameters are lower then those currently used in models. The data presented here are a first step toward the accurate measurement of the major driver of photochemical air pollution, the photolysis rate parameters. Although photolysis rate parameters and actinic flux have been measured in past field studies these measurements are the first conducted as part of a major field study within California made for both scientific and regularly applications.

9. References

Atkinson, R., Gas-phase tropospheric chemistry of organic compounds: a review, *J. Phys. Chem. Ref. Data*, Monograph 2, 1-216, 1994.

Cantrell, C.A., J.A. Davidson, A.H. McDaniel, R.E. Shetter and J.G. Calvert, Temperature-dependent formaldehyde cross sections in the near-ultraviolet spectral region, *J. Phys. Chem.*, *94*, 3902-3908, 1990.

Cvetanovic R.J. R.P. Overend and G. Parakevoponlos, *Int. J. Chemical Kinetics, 7*, 249, 1975

DeMore, W.B., S.P. Sander, D.M. Golden, R.F. Hampson, M.J. Kurylo, C.J. Howard, A.R. Ravishankara, C.E. Kolb and M.J. Molina *Chemical Kinetics and Photochemical Data for Use in Stratospheric Modeling*, *Evaluation Number 11*, National Aeronautics and Space Administration, Jet Propulsion Laboratory, California Institute of Technology, Pasadena, California, 1994.

DeMore,W.B., S.P.Sander,D.M. Golden, R.F.Hampson, M.J.Kurylo, C.J.Howard, A.R. Ravishankara, C.E. Kolb and M.J. Molina, Chemical Kinetics and Photochemical Data for Use in Stratospheric Modeling, Evaluation Number 12, National Aeronautics and Space Administration, Jet Propulsion Laboratory, California Institute of Technology, Pasadena, California, 1997.

Finlayson-Pitts, B.J., Pitts, J.N., *Chemistry of the Upper and Lower Atmosphere: Theory, Experiments, and Applications*, Academic Press, New York, 1999.

Jacobson, M.Z., *Fundamentals of Atmospheric Modeling*, Cambridge University Press, Cambridge, 1999.

Joseph, J.H., Wiscombe, W.J., The delta-Eddington approximation for radiative flux transfer. *J. Atmos. Science*, *33*, 2452-2459, 1976.

Madronich, S., Photodissociation in the atmosphere; 1. Actinic flux and the effects on ground reflections and clouds, *J. Geophys. Res.*, 92, 9740-9752, 1987.

Molina L.T. and M.J. Molina, Absolute absorption cross sections of ozone in the 185-350 nm wavelength range, J.Geophys Res., 91, 14501-14508, 1986.

Moortgat, G.K., W. Klippel, K.H. Mobus, W. Seiler and P. Warneck, *Laboratory measurement of photolytic parameters for formaldehyde, Final Rep. FAA-EE-80-47*, Off. of Environ. and Energy, Fed Aviat. Admin., Washington D.C., 1980.

Sander, S.P., R.R. Friedl, W.B. DeMore, A.R. Ravishankara, D.M. Golden, C.E. Kolb, M.J. Kurylo, R.F. Hampson, R.E. Huie, M.J. Molina, G.K. Moortgat, Chemical Kinetics and Photochemical Data for Use in Stratospheric Modeling, Supplement to Evaluation 12: Update of Key Reactions, Evaluation Number 13, JPL Publication 00-3,Jet Propulsion Laboratory, California Institute of Technology, Pasadena, California, 2000.

Appendix A Description of Disk with Photolysis Rate Parameter Data

Disk labels

The disk containing the photolysis rate parameter data provided to ARB includes directories for each site and reaction, Table A-1.

Table A-1. Reactions and files provided on data provided with report.

Reaction	Directory
$NO_2 + h\nu \rightarrow NO + O(^3P)$	JNO2_UC_Davis JNO2_Sunol JNO2_DRI
$O_3 + h\nu \rightarrow O_2 + O(^1D)$	JO3_UC_Davis JO3_Sunol JO3_DRI
$HCHO + h\nu \rightarrow H_2 + CO$	JHCHO_Mol_UC_Davis JHCHO_Mol_Sunol JHCHO_Mol_DRI
$HCHO + h\nu (+ O_2) \rightarrow 2\ HO_2 + CO$	JHCHO_Rad_UC_Davis JHCHO_Rad_Sunol JHCHO_Rad_DRI

Each file in the directories indicated the reaction and the month or months of the date. For example, JO3_September_Sunol indicates a file for the photolysis rate parameters of ozone measured at Sunol for the month of September. Within each file the date follow the format: date, hour and value. The times of the spectra, hour, minute and second in Pacific Standard Time (PST).

Table A-2. Format of photolysis rate parameter files provided. File JNO2_July_UC_Davis.txt is used as the example.

Date	**Time (PST)**	**Photolysis Rate Parameter (s^{-1})**
07/21/2000	12:00:04.8	0.6188084799E-02